Journal of Computational Physics 229 (2010) 3019–3045

Contents lists available at ScienceDirect

Journal of Computational Physics

journal homepage: www.elsevier.com/locate/jcp

BDF-like methods for nonlinear dynamic analysis

S. Dong

Center for Computational and Applied Mathematics, Department of Mathematics, Purdue University, 150 N. University Street, West Lafayette 47907, USA

ARTICLE INFO

Article history:
Received 17 June 2009
Received in revised form 12 October 2009
Accepted 23 December 2009
Available online 4 January 2010

Keywords:
Nonlinear dynamics
Time integration
Backward differentiation formula

ABSTRACT

We present several time integration algorithms of second-order accuracy that are numerically simple and effective for nonlinear elastodynamic problems. These algorithms are based on a general four-step scheme that has a resemblance to the backward differentiation formulas. We also present an extension to the composite strategy of the Bathe method. Appropriate values for the algorithmic parameters are determined based on considerations of stability and dissipativity, and less dissipative members of each algorithm have been identified. We demonstrate the convergence characteristics of the proposed algorithms with a nonlinear dynamic problem having analytic solutions, and test these algorithms with several three-dimensional nonlinear elastodynamic problems involving large deformations and rotations, employing St. Venant-Kirchhoff and compressible Neo-Hookean hyperelastic material models. These tests show that stable computations are obtained with the proposed algorithms in nonlinear situations where the trapezoidal rule encounters a well-known instability.

1. Introduction

The failure of popular algorithms in nonlinear dynamic analysis, e.g. the loss of unconditional stability of the trapezoidal rule in the nonlinear regime [32,40,26,1], has motivated much of recent work in the development of more robust time integration algorithms for nonlinear elastodynamics. As pointed out in [25], numerical stability is of primary importance when developing such schemes. In this regard, energy-conserving algorithms (e.g. [22,36,26,23,17,8,34,29,33]) that target nonlinear problems have been proposed by a number of researchers. Among them the energy-momentum type methods pioneered by Simo and Tarnow [36], with improvements and extensions by many subsequent efforts (see e.g. [37,26,25,17,28], among others), have been especially successful. However, energy-conserving schemes have shown difficulties for numerically stiff problems due to their lack of dissipation in the high-frequency range. Failures of energy-conserving algorithms have been reported in [31,6,26,27,2], among others. It has been realized that the numerical instabilities associated with the existence of repeated unit root at infinite frequency in common conserving schemes result in highly oscillatory responses, which hinder the convergence process for the solution of nonlinear equations [2]. Reducing the time step size may not necessarily help the convergence process as a smaller time step may allow the excitation of even higher frequencies [5]. As a result, the need for numerical dissipation in the high-frequency range, even though the underlying system may exhibit full energy conservation, has been commonly recognized for robust time integration algorithms in the nonlinear regime.

Classical dissipative schemes [30,38,20,39,9] have been developed in the context of linear elastodynamics, see [21] for a more comprehensive description. Although they have also been applied to nonlinear problems, it is observed that these algorithms fail to provide reliable high-frequency dissipation in the nonlinear regime [25,2]. Indeed, the value of the algorithmic parameter at which the scheme is dissipative may become problem dependent, see [19] for such an example in the nonlinear

E-mail address: sdong@math.purdue.edu

0021-9991/$ - see front matter © 2009 Elsevier Inc. All rights reserved.
doi:10.1016/j.jcp.2009.12.028

regime with the HHT-α scheme [20]. Much of recent research work [26,25,7,2,5,19] aiming to provide reliable numerical dissipation in the nonlinear regime has been motivated by the ineffectiveness of classical dissipative schemes for nonlinear problems. Most of the recently proposed algorithms are constructed based on some energy-conserving scheme, or other approaches such as the time discontinuous Galerkin method.

Another interesting approach has recently been proposed by Bathe and collaborators [3,4]. The main idea is to combine the trapezoidal rule and the second-order backward Euler method into a composite algorithm. High-frequency numerical dissipation is introduced through the backward Euler component. The algorithm has been demonstrated to be effective for nonlinear elastodynamic problems involving large deformations, where the trapezoidal rule fails to produce a stable solution. The simplicity of this approach is particularly noteworthy, together with the symmetry of the resultant tangential stiffness matrix, which is to be contrasted with the non-symmetry of the tangent matrices resulting from, for example, the energy-momentum based methods.

In this paper we propose a general four-step scheme that bears a resemblance to the backward differentiation formulas (BDF) [16], and present two time integration algorithms based on this scheme. We also consider a composite algorithm incorporating such a BDF-like scheme and the trapezoidal rule using a composite strategy similar to the Bathe method [3], and also present an extension of the Bathe composite strategy. These algorithms each involve two algorithmic parameters. The domains of the appropriate parameter values are determined based on a linear stability analysis and the consideration of dissipativity. Although a nonlinear stability analysis of these algorithms for general nonlinear elastodynamic problems is still elusive, numerical experiments suggest that these algorithms are very effective for nonlinear dynamic problems at time step sizes where the trapezoidal rule encounters a well-known instability. We test these algorithms for several three-dimensional (3D) nonlinear elastodynamic problems involving large deformations with St. Venant-Kirchhoff and compressible Neo-Hookean material models. The convergence characteristics of these algorithms are demonstrated using a nonlinear problem having analytic solutions.

The rest of this paper is organized as follows. In Section 2 we briefly discuss the high-order spatial discretization scheme of the nonlinear elastodynamic equation with the spectral element method, which has been documented in detail elsewhere [15]. The proposed temporal algorithms will be implemented and tested in conjunction with this approach for spatial discretization. In Section 3 we present a general four-step BDF-like scheme with second-order accuracy, and several algorithms based on this scheme. In Section 4 we demonstrate the temporal convergence characteristics of these algorithms with a nonlinear problem having analytic solutions. In Section 5 we test the proposed algorithms with several nonlinear elastodynamic problems involving large deformations for St. Venant-Kirchhoff and Neo-Hookean hyperelastic materials, and compare them with the trapezoidal rule, the Bathe method, and the Park method [32]. Finally, Section 6 provides some concluding remarks.

2. Problem formulation

Consider the finite deformation of a 3D object occupying domain Ω with boundary $\partial\Omega = \partial\Omega_D \cup \partial\Omega_N$, where Dirichlet boundary conditions (BC) are provided on $\partial\Omega_D$ and Neumann-type (traction) BCs on $\partial\Omega_N$. Assume that the object is in its natural configuration (no deformation), Ω_0, at time $t = 0$, and deforms to a new configuration, $\Omega(t)$, at time t. With respect to the initial configuration Ω_0, the weak form of the momentum equation can be expressed as follows,

$$\int_{\Omega_0} \mathbf{S} : \frac{1}{2}\left(\left(\frac{\partial \mathbf{v}}{\partial \mathbf{X}}\right)^T \cdot \mathbf{F}(\mathbf{u}) + \mathbf{F}^T(\mathbf{u}) \cdot \frac{\partial \mathbf{v}}{\partial \mathbf{X}}\right) d\Omega_0 - \int_{\partial\Omega_{0N}} \mathbf{T} \cdot \mathbf{v} d\Gamma - \int_{\Omega_0} \rho_0 \mathbf{f} \cdot \mathbf{v} d\Omega_0 + \int_{\Omega_0} \rho_0 \frac{\partial^2 \mathbf{u}}{\partial t^2} \cdot \mathbf{v} d\Omega_0 = 0 \quad \forall \mathbf{v} \in \mathbf{V}_0, \tag{1}$$

where $\mathbf{X}$ is the coordinate in Ω_0, $\mathbf{u}(\mathbf{X}, t)$ is the displacement, and $\mathbf{V}_0 = \{\mathbf{w}(\mathbf{X}) \in [H^1(\Omega_0)]^3 | \mathbf{w}(\mathbf{X}) = 0 \text{ on } \partial\Omega_{0D}\}$. In the above equation, $\mathbf{S}$, $\mathbf{F}(\mathbf{u})$, $\mathbf{f}$ and ρ_0 are, respectively the second Piola–Kirchhoff stress tensor, deformation gradient tensor, external body force, and the structural mass density in the initial configuration. The external traction force $\mathbf{T}$ is assumed to be deformation-independent, i.e. non-follower load. The superscript in $(\cdot)^T$ denotes transposition.

We consider two hyperelastic material models in this paper. The first model is the St. Venant-Kirchhoff constitutive law, which is characterized by the following strain energy density function

$$\Psi = \frac{\lambda}{2}(\mathrm{tr}\mathbf{E})^2 + \mu \mathbf{E} : \mathbf{E}, \tag{2}$$

where $\mathbf{E}$ is the Green-Lagrange strain tensor; λ and μ are material constants, related to the Young's modulus E and Poisson ratio v by

$$\lambda = \frac{vE}{(1+v)(1-2v)}, \quad \mu = \frac{E}{2(1+v)}. \tag{3}$$

We will also consider a compressible Neo-Hookean material, characterized by the following strain energy density function

$$\Psi = \frac{\mu}{2}(I_{\mathbf{C}} - 3) - \mu \log J + \frac{\lambda}{2}(\log J)^2, \tag{4}$$

where $\mathbf{C}$ is the right Cauchy-Green deformation tensor, J is the Jacobian ($J^2 = \det \mathbf{C}$), $I_{\mathbf{C}} = \mathrm{tr}\mathbf{C}$, and μ and λ are material constants.

In the numerical examples presented in Section 5 we will extensively investigate the characteristics of the total energy, defined by

$$H = \int_{\Omega_0} \frac{1}{2}\rho_0 \left(\frac{\partial \mathbf{u}}{\partial t}\right)^2 d\Omega_0 + \int_{\Omega_0} \Psi d\Omega_0 \tag{5}$$

and the angular momentum, defined by

$$\mathbf{J} = \int_{\Omega_0} \rho_0 (\mathbf{X} + \mathbf{u}) \times \frac{\partial \mathbf{u}}{\partial t} d\Omega_0. \tag{6}$$

We employ a high-order spectral element approach (see [15] for details) to discretize Eq. (1) spatially. The essential component of this approach is a set of high-order shape functions based on Jacobi polynomials for unstructured elements, which provides a unified treatment for all commonly encountered element types in 3D space (hexahedron, tetrahedron, prism, pyramid). These shape functions were originated from computational fluid dynamics [35,24], and have been employed to solve Navier–Stokes equations and turbulence problems [12,13,11,10,14]. New schemes for temporal discretization will be proposed and discussed below in Section 3. The spatial and temporal discretization processes result in a set of nonlinear algebraic equations, which will be solved with a Newton–Raphson iterative procedure [15].

3. Time integration algorithms

After spatial discretization of Eq. (1), we obtain a semi-discretized equation,

$$\mathbf{M}\ddot{\mathbf{U}} + \mathbf{N}(\mathbf{U}, t) - \mathbf{R}(t) = 0, \tag{7}$$

where overdot denotes the time derivative; **M** and **U** are, respectively the mass matrix and the vector of expansion coefficients of the displacement; **N** represents the contribution of the internal stresses, and is nonlinear with respect to the displacement; **R** represents the contribution of the external loads. Note that **R** does not depend on **U** under the assumption of non-follower loads we made in Section 2. This equation is supplemented with appropriate initial conditions. We will enforce Eq. (7) at time step $(n+1)$, i.e.

$$\mathbf{M}\ddot{\mathbf{U}}^{n+1} + \mathbf{N}^{n+1} - \mathbf{R}^{n+1} = 0, \tag{8}$$

where n is the time step index.

In this section we propose a general four-step BDF-like scheme, and several temporal algorithms based on this scheme for solving Eq. (7). Each algorithm involves two parameters, and we determine the appropriate values of these parameters based on a linear stability analysis. So the term stability used in this section is confined to the linear sense.

3.1. A BDF-like scheme of second-order accuracy

We propose the following general four-step linear multistep scheme, in the spirit of backward differentiation formulas, for solving the semi-discretized equation,

$$\alpha_1 y^{n+1} + \alpha_2 y^n + \left(\frac{7}{2} - 6\alpha_1 - 3\alpha_2\right) y^{n-1} + (8\alpha_1 + 3\alpha_2 - 6) y^{n-2} + \left(\frac{5}{2} - 3\alpha_1 - \alpha_2\right) y^{n-3} = \dot{y}^{n+1}\Delta t, \tag{9}$$

where y is a generic variable.

The algorithmic parameters α_1 and α_2 are real numbers $(\alpha_1 \neq 0)$. The time step size Δt is assumed to be constant. One can demonstrate that this scheme has a temporal second-order accuracy for all (α_1, α_2) values by employing the order condition for linear multistep schemes [18]. Requiring the scheme to be stable as $\Delta t \to 0$ (i.e. zero-stability) leads to the following conditions on the parameters

$$\begin{cases} \alpha_2 \leqslant -2\alpha_1 + \frac{3}{2} \\ \alpha_2 > -\frac{18}{5}\alpha_1 + \frac{5}{2}. \end{cases} \tag{10}$$

3.1.1. Restriction to a three-step scheme

We first restrict this scheme to a three-step type (with $\alpha_2 = \frac{5}{2} - 3\alpha_1$),

$$\alpha_1 y^{n+1} + \left(\frac{5}{2} - 3\alpha_1\right) y^n + (3\alpha_1 - 4) y^{n-1} + \left(\frac{3}{2} - \alpha_1\right) y^{n-2} = \dot{y}^{n+1}\Delta t, \tag{11}$$

and accordingly with the zero-stability condition $\alpha_1 \geqslant 1$. It is straightforward to check that $\alpha_1 = 3/2$ corresponds to the second-order BDF (BDF2) and $\alpha_1 = 11/6$ corresponds to the third-order BDF (BDF3). To facilitate subsequent discussions we reparametrize the above scheme with the transform $\alpha_1 = \frac{11}{6} - \frac{\theta}{3}$, and Eq. (11) becomes

$$A(\theta) y^{n+1} + B(\theta) y^n + C(\theta) y^{n-1} + D(\theta) y^{n-2} = \dot{y}^{n+1}\Delta t, \tag{12}$$

where

$$\begin{cases} A(\theta) = \frac{11}{6} - \frac{\theta}{3}, \\ B(\theta) = \theta - 3, \\ C(\theta) = \frac{3}{2} - \theta, \\ D(\theta) = -\frac{1}{3} + \frac{\theta}{3}. \end{cases} \tag{13}$$

The zero-stability condition for the re-parametrized scheme is given by $\theta \leqslant \frac{5}{2}$.

In the first algorithm we employ the scheme represented by Eq. (12), but discretize the velocity and acceleration in a different yet complementary fashion as follows:

$$\dot{\mathbf{U}}^{n+1} = \frac{A(\theta_1)}{\Delta t}\mathbf{U}^{n+1} + \frac{B(\theta_1)}{\Delta t}\mathbf{U}^{n} + \frac{C(\theta_1)}{\Delta t}\mathbf{U}^{n-1} + \frac{D(\theta_1)}{\Delta t}\mathbf{U}^{n-2} \tag{14}$$

$$\ddot{\mathbf{U}}^{n+1} = \frac{A(\theta_2)}{\Delta t}\dot{\mathbf{U}}^{n+1} + \frac{B(\theta_2)}{\Delta t}\dot{\mathbf{U}}^{n} + \frac{C(\theta_2)}{\Delta t}\dot{\mathbf{U}}^{n-1} + \frac{D(\theta_2)}{\Delta t}\dot{\mathbf{U}}^{n-2} \tag{15}$$

where the algorithmic parameters θ_1 and θ_2 in general may take different values, with $\theta_1, \theta_2 \leqslant \frac{5}{2}$ according to the zero-stability condition. We will refer to this method as the GBDF-A algorithm in subsequent discussions.

We aim to seek (θ_1, θ_2) values such that the algorithm represented by Eqs. (14) and (15) is linearly unconditionally stable and with relatively low dissipativity. For this purpose we first consider the scalar free-oscillation equation with no damping:

$$\ddot{u} + \omega^2 u = 0 \tag{16}$$

with initial conditions $u(0) = 1$ and $\dot{u}(0) = 0$, where u is the scalar variable to be solved and $\omega > 0$ is the angular frequency of oscillation. We discretize Eq. (16) employing the scheme represented by Eqs. (14) and (15), and obtain the iterative relation:

$$[u^{n+1}\ u^{n}\ u^{n-1}\ \dot{u}^{n+1}\ \dot{u}^{n}\ \dot{u}^{n-1}]^T = \mathbf{G}[u^{n}\ u^{n-1}\ u^{n-2}\ \dot{u}^{n}\ \dot{u}^{n-1}\ \dot{u}^{n-2}]^T, \tag{17}$$

where $\mathbf{G}$ is the amplification matrix and its specific form is provided in Appendix A.

The eigenvalues $\lambda_i (i = 1, \ldots, 6)$, and the spectral radius $\rho_{\mathbf{G}}$, of the amplification matrix are functions of θ_1 and θ_2, and depend on ω and Δt only through the term $\omega\Delta t$. In Fig. 1(a) we plot contours in the θ_1–θ_2 plane of the maximum spectral radius, $\rho_{\max}(\theta_1, \theta_2) = \max_{0 \leqslant \omega\Delta t < \infty} \rho_{\mathbf{G}}(\theta_1, \theta_2, \omega\Delta t)$. In the shaded region of this plot, the maximum spectral radius has a unit value for any time step size $0 \leqslant \frac{\Delta t}{T} < \infty$, where T is the period of oscillation, $T = 2\pi/\omega$. This region is bounded by the lines $\theta_1 = 5/2$ and $\theta_2 = 5/2$ on the right and top sides, and by the line $\theta_1 + \theta_2 = 1 (-0.2 \lesssim \theta_1 \lesssim 1.2, -0.2 \lesssim \theta_2 \lesssim 1.2)$, in the middle portion of the left-bottom side.

We next investigate the distribution of all the eigenvalues of the amplification matrix in the complex plane for (θ_1, θ_2) values residing in this shaded region. Fig. 1(b) shows the distribution of the six eigenvalues in the complex plane corresponding to $(\theta_1, \theta_2) = (1, 0)$, as $\omega\Delta t$ increases from zero to ∞ (The largest $\omega\Delta t$ value computed in the figure is 2000π). The arrows

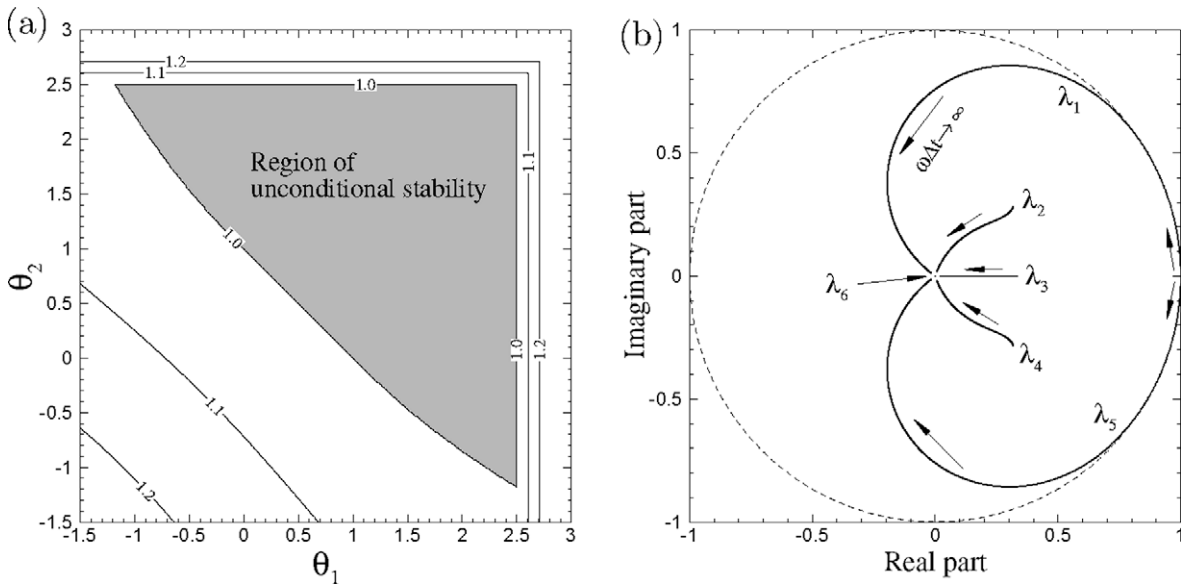

Fig. 1. GBDF-A algorithm (damping-free equation): (a) contours of maximum spectral radius (for $0 \leqslant \frac{\Delta t}{T} < \infty$) in θ_1–θ_2 plane; (b) distribution of eigenvalues of the amplification matrix in the complex plane for $0 \leqslant \omega\Delta t < \infty$ with $(\theta_1, \theta_2) = (1, 0)$. The arrows near the curves indicate how the eigenvalues evolve as $\omega\Delta t$ increases. The test problem is the free vibration of a spring (no damping). T is the period of vibration, $T = \frac{2\pi}{\omega}$.

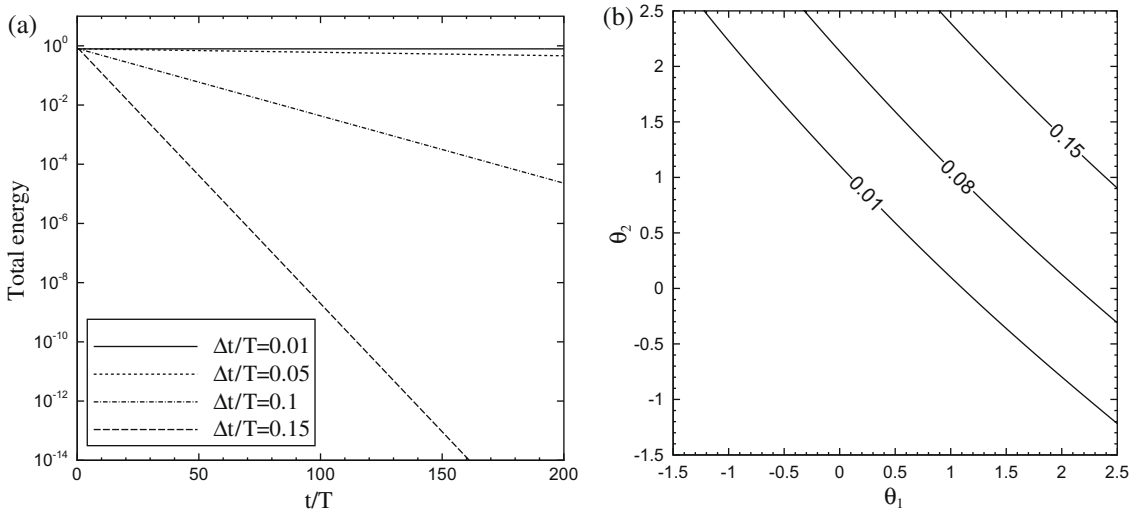

Fig. 2. Dissipativity of GBDF-A algorithm: (a) history of the total energy for linear vibration equation computed with $(\theta_1, \theta_2) = (1/2, 1/2)$ and different time step sizes and (b) contours of fraction of energy loss per period, at a fixed $\frac{\Delta t}{T} = 0.05$, in $\theta_1 - \theta_2$ plane.

near each curve indicate how the eigenvalues evolve with increasing $\omega\Delta t$. The dashed line marks the unit circle in the plane. On can observe that all eigenvalues approach zero at large $\omega\Delta t$ values. A pair of complex eigenvalues (λ_1 and λ_5 in Fig. 1(b), conjugate to each other) originate from the point (1,0), which corresponds to $\omega\Delta t = 0$. They have the largest norm among the six eigenvalues as $\omega\Delta t$ is small. Another conjugate pair of complex eigenvalues (λ_2 and λ_4) originate from inside the unit circle. The two remaining eigenvalues are real, and λ_6 is identically zero. The key observation here is that for any $\omega\Delta t > 0$ all eigenvalues have a norm not larger than the unit value, and that there is no repeated eigenvalue (i.e. multiplicity more than one) with a unit norm. For other θ_1, θ_2 values in the shaded region, the shapes of the eigenvalue curves in the complex plane differ from those of Fig. 1(b) to a certain degree. For example, three pairs of complex eigenvalues result from some θ_1, θ_2 values. However, the observation that no eigenvalue is repeated with a unit norm for $\omega\Delta t > 0$ is always true. This indicates that the GBDF-A algorithm with parameters θ_1, θ_2 located in the shaded region of Fig. 1(a) is linearly unconditionally stable.

We next investigate the effect of (θ_1, θ_2) values on the dissipativity of the GBDF-A algorithm. The total energy of the linear vibration, defined by $E_t = \frac{1}{2}\omega^2 u^2 + \frac{1}{2}\dot{u}^2$, decays over time as a function, $E_t = E_0 e^{-\gamma t/T}$, where E_0 is the initial energy and the constant γ depends on θ_1, θ_2 and $\Delta t/T$, as is shown by the total energy histories in Fig. 2(a). We therefore employ the fraction of energy loss per period, $\frac{E_0 - E_t|_{t=T}}{E_0} = 1 - e^{-\gamma}$, as a measure of the dissipativity of the algorithm. In Fig. 2(b) we plot contours of the fraction of energy loss per period, $1 - e^{-\gamma}$, for a fixed $\Delta t/T = 0.05$, over the region of unconditional stability in the θ_1 and θ_2 plane. It shows that as (θ_1, θ_2) moves away from the left-bottom boundary toward the top-right of the domain of unconditional stability, the algorithm becomes more dissipative. The parameter values on the line $\theta_1 + \theta_2 = 1$ are therefore among the least dissipative of this class of schemes, and are preferred in terms of dissipativity. Note that for the GBDF-A scheme with $\theta_1 + \theta_2 = 1 (-0.2 \lesssim \theta_1, \theta_2 \lesssim 1.2)$ the velocity and the acceleration are discretized in a different but complementary fashion (see Eqs. (14) and (15)). In particular, with $(\theta_1, \theta_2) = (1, 0)$ the velocity is discretized with BDF2 while the acceleration is discretized with BDF3; With $(\theta_1, \theta_2) = (0, 1)$ the velocity is discretized with BDF3 while the acceleration is discretized with BDF2. Note that BDF3 itself is not unconditionally stable. But when BDF3 and BDF2 are combined in the above fashion the overall algorithm is unconditionally stable due to their interactions. The GBDF-A scheme with $\theta_1, \theta_2 = (1/2, 1/2)$ corresponds to the Park method [32].

The GBDF-A algorithm with parameters (θ_1, θ_2) residing in the domain of unconditional stability is also stable in the presence of physical damping. To demonstrate this point we consider the damped linear vibration equation

$$\ddot{u} + 2\xi\omega\dot{u} + \omega^2 u = 0, \tag{18}$$

where ξ is the damping coefficient. Applying the GBDF-A scheme to this equation, we can similarly form the amplification matrix. Fig. 3 shows typical spectral radii plots and the eigenvalue distributions in the complex plane for the damped vibration equation, which are computed with $(\theta_1, \theta_2) = (1, 0)$. Fig. 3(a) is a plot of the spectral radii of the amplification matrix as a function of the time step size for several damping coefficient values, ranging from no damping, to critical damping and over-damping situations. It shows that the spectral radius is no larger than the unit value for any $\Delta t/T$. Examination of the eigenvalue distribution in the complex plane for different ξ values further indicates that no eigenvalue is repeated with a unit norm for any $\Delta t/T > 0$. This is demonstrated in Fig. 3(b) by the eigenvalue distribution as $\Delta t/T \to \infty$ for a fixed damping coefficient $\xi = 0.1$. A comparison between Fig. 3(b) and 1(b) (no damping) indicates that the presence of physical damping has moved the largest eigenvalues (λ_1 and λ_5) inward toward the origin, making the computation more stable. With a larger

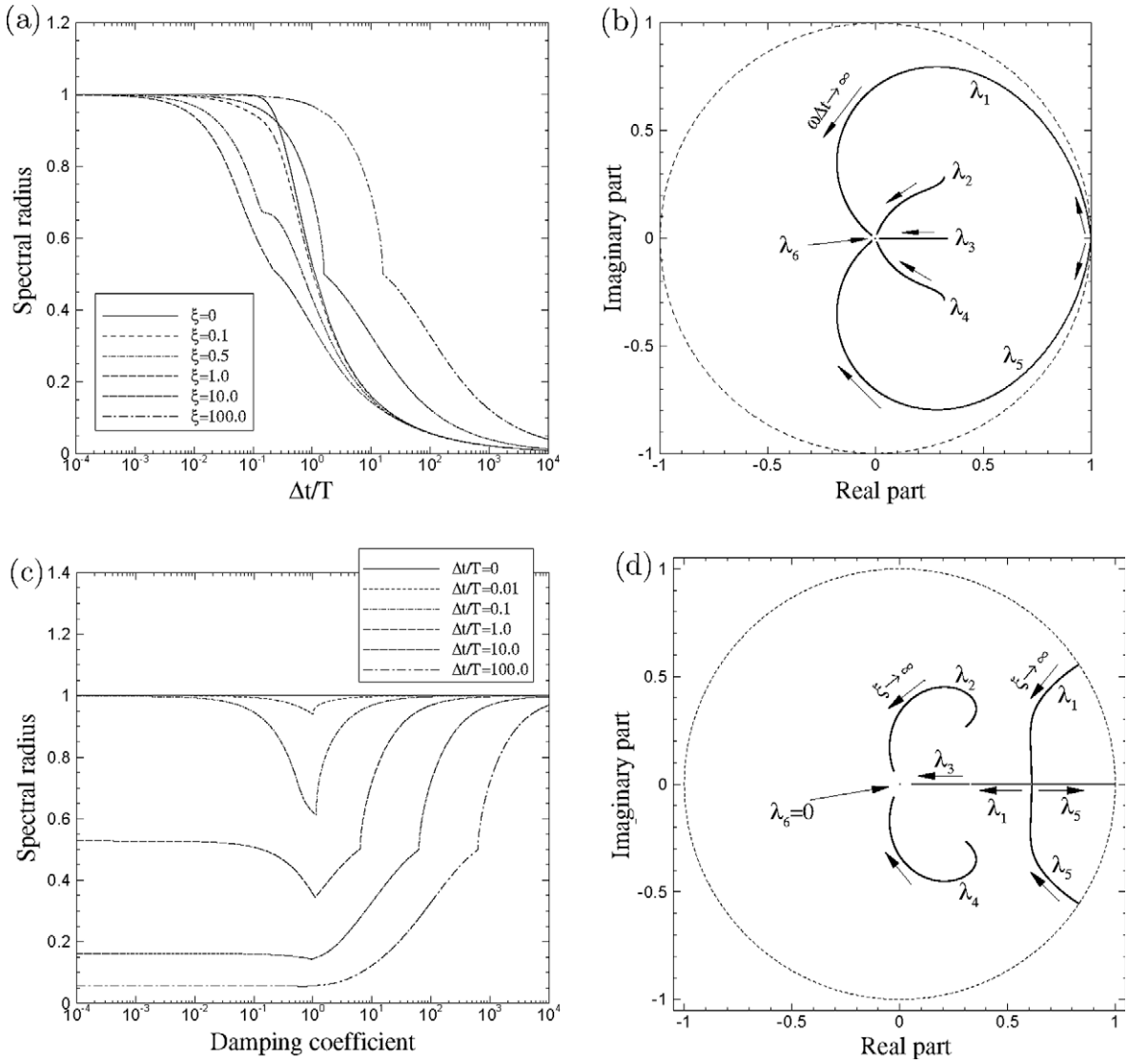

Fig. 3. GBDF-A algorithm (damped vibration equation): (a) spectral radii of the amplification matrix versus time step size $\Delta t/T$ for various damping coefficients ξ, (b) eigenvalue distribution in complex plane as $\Delta t/T \to \infty$ for a fixed $\xi = 0.1$, (c) spectral radii versus ξ for various $\Delta t/T$ and (d) eigenvalue distribution in complex plane as $\xi \to \infty$ for a fixed $\Delta t/T = 0.1$. All results correspond to $(\theta_1, \theta_2) = (1.0, 0.0)$.

damping coefficient ξ, the distribution moves further toward the origin. It is evident that the amplification matrix has no repeated eigenvalue with a unit norm for any $\Delta t/T \neq 0$. Fig. 3(c) shows the spectral radii as a function of the damping coefficient ξ for several fixed time step sizes $\Delta t/T$, and Fig. 3(d) shows the eigenvalue distribution in the complex plane as $\xi \to \infty$ with a fixed $\Delta t/T = 0.1$. The arrows near each curve in Fig. 3(d) indicate how the eigenvalues evolve with the increase of ξ. Most notably, the pair of complex eigenvalues with the largest norm (λ_1 and λ_5) evolve into two distinct real eigenvalues at large ξ values. While λ_1 moves toward the origin, λ_5 approaches the unit value as $\xi \to \infty$. The amplification matrix has no repeated eigenvalue with a unit norm for any $\xi \geqslant 0$. The above observations also apply to other (θ_1, θ_2)values in the shaded region of Fig. 1(a). These results demonstrate the unconditional stability of the GBDF-A scheme in the presence of physical damping.

We herein propose to employ the GBDF-A algorithm represented by Eqs. (14) and (15) to solve the semi-discretized nonlinear elastodynamic Eq. (8), with the requirement that the algorithmic parameters (θ_1, θ_2) should reside in the region of unconditional stability. Eliminating $\dot{\mathbf{U}}^{n+1}$ from Eqs. (14) and (15), and substituting the resulting expression for $\ddot{\mathbf{U}}^{n+1}$ into Eq. (8) will lead to a nonlinear algebraic equation about $\mathbf{U}^{n+1}$, which can be solved with a Newton-type method. Subsequently $\dot{\mathbf{U}}^{n+1}$ and $\ddot{\mathbf{U}}^{n+1}$ can be obtained by using Eqs. (14) and (15). The performance of the GBDF-A algorithm for nonlinear dynamic problems will be demonstrated in Section 5 with numerical examples.

3.1.2. General four-step scheme

Let us now consider the general four-step scheme of Eq. (9) for the semi-discretized elastodynamic equation. We re-parametrize the scheme with the following transform,

$$\begin{cases} \alpha_1 = -\frac{1}{3}\theta_1\theta_2 - \frac{1}{4}\theta_2 + \frac{25}{12} \\ \alpha_2 = \theta_1\theta_2 + \theta_2 - 4. \end{cases} \tag{19}$$

Accordingly, Eq. (9) is transformed to

$$A_1(\theta_1,\theta_2)y^{n+1} + A_2(\theta_1,\theta_2)y^n + A_3(\theta_1,\theta_2)y^{n-1} + A_4(\theta_1,\theta_2)y^{n-2} + A_5(\theta_1,\theta_2)y^{n-3} = \dot{y}^{n+1}\Delta t, \tag{20}$$

where

$$\begin{cases} A_1(\theta_1,\theta_2) = -\frac{1}{3}\theta_1\theta_2 - \frac{1}{4}\theta_2 + \frac{25}{12}, \\ A_2(\theta_1,\theta_2) = \theta_1\theta_2 + \theta_2 - 4, \\ A_3(\theta_1,\theta_2) = -\theta_1\theta_2 - \frac{3}{2}\theta_2 + 3, \\ A_4(\theta_1,\theta_2) = \frac{1}{3}\theta_1\theta_2 + \theta_2 - \frac{4}{3}, \\ A_5(\theta_1,\theta_2) = \frac{1}{4} - \frac{1}{4}\theta_2. \end{cases} \tag{21}$$

The zero-stability condition is transformed to the following relation

$$\begin{cases} (\theta_1 + \frac{3}{2})\theta_2 \leqslant 4 \\ (\theta_1 - \frac{1}{2})\theta_2 < 5. \end{cases} \tag{22}$$

For temporal discretization of the semi-discretized elastodynamic equation we employ the above scheme as follows,

$$\begin{cases} \dot{\mathbf{U}}^{n+1} = \frac{A_1(\theta_1,\theta_2)}{\Delta t}\mathbf{U}^{n+1} + \frac{A_2(\theta_1,\theta_2)}{\Delta t}\mathbf{U}^{n} + \frac{A_3(\theta_1,\theta_2)}{\Delta t}\mathbf{U}^{n-1} + \frac{A_4(\theta_1,\theta_2)}{\Delta t}\mathbf{U}^{n-2} + \frac{A_5(\theta_1,\theta_2)}{\Delta t}\mathbf{U}^{n-3} \\ \ddot{\mathbf{U}}^{n+1} = \frac{A_1(\theta_1,\theta_2)}{\Delta t}\dot{\mathbf{U}}^{n+1} + \frac{A_2(\theta_1,\theta_2)}{\Delta t}\dot{\mathbf{U}}^{n} + \frac{A_3(\theta_1,\theta_2)}{\Delta t}\dot{\mathbf{U}}^{n-1} + \frac{A_4(\theta_1,\theta_2)}{\Delta t}\dot{\mathbf{U}}^{n-2} + \frac{A_5(\theta_1,\theta_2)}{\Delta t}\dot{\mathbf{U}}^{n-3} \end{cases} \tag{23}$$

The algorithm represented by the above equation will be referred to as the GBDF-B scheme in subsequent discussions.

We are interested in the values of (θ_1,θ_2) such that this algorithm (Eq. (23)) is linearly unconditionally stable. A spectral analysis using the damping-free linear vibration Eq. (16) similar to the previous section results in the following iterative relation:

$$\left[u^{n+1}\ u^n\ u^{n-1}\ u^{n-2}\ \dot{u}^{n+1}\ \dot{u}^n\ \dot{u}^{n-1}\ \dot{u}^{n-2}\right]^T = \mathbf{G}\left[u^n\ u^{n-1}\ u^{n-2}\ u^{n-3}\ \dot{u}^n\ \dot{u}^{n-1}\ \dot{u}^{n-2}\ \dot{u}^{n-3}\right]^T. \tag{24}$$

The specific form of the amplification matrix $\mathbf{G}$ is provided in Appendix A.

Fig. 4(a) shows in the $\theta_1 - \theta_2$ plane contours of the maximum spectral radius $\rho_{\max}(\theta_1,\theta_2) = \max_{0\leqslant\frac{\Delta t}{T}<\infty}\rho_{\mathbf{G}}(\theta_1,\theta_2,\omega\Delta t)$, where T is the period of vibration, $T = 2\pi/\omega$, and $\rho_{\mathbf{G}}(\theta_1,\theta_2,\omega\Delta t)$ is the spectral radius of the amplification matrix. Within the shaded region in Fig. 4(a) $\rho_{\max}$ has an identical unit value.

For (θ_1,θ_2) values from the shaded region, eigenvalue distribution indicates that the amplification matrix has no repeated eigenvalue of a unit norm. This is shown in Fig. 4(b) by the distribution of the eight eigenvalues in the complex plane corresponding to $(\theta_1,\theta_2) = (1/2, 4/5)$, which belongs to this region. The matrix has four complex conjugate pairs of eigenvalues. Among them the pair of λ_1 and λ_8 originates from the point (1,0) in the complex plane (which corresponds to $\omega\Delta t = 0$) and has the largest norm as $\omega\Delta t$ is not large, while the other eigenvalues all originate from and are confined inside the unit circle. One can observe that for any $\omega\Delta t > 0$ the norms of all eigenvalues are no larger than one and that no eigenvalue is repeated with a unit norm. This observation also applies to other (θ_1,θ_2) values from the shaded region of Fig. 4(a). Therefore, the shaded region corresponds to the domain of unconditional stability of the GBDF-B algorithm. Note that this domain is non-compact in the $\theta_1 - \theta_2$ plane, and it is contained within the domain of zero-stability (Eq. (22)). The left boundary of this domain lies on the line $\theta_1 = \frac{1}{2}$ (with $4/5 \leqslant \theta_2 \leqslant 2$). A study of the damped vibration Eq. (18) shows that the GBDF-B algorithm with (θ_1,θ_2) values located in this domain is also unconditionally stable in the presence of physical damping.

The dissipativity characteristics of the GBDF-B algorithm is demonstrated by Fig. 4(c), in which we plot contours of the fraction of energy loss per period in the $\theta_1 - \theta_2$ plane, computed using a time step size $\Delta t/T = 0.02$. A comparison of Fig. 4(a) and (c) indicates that within the domain of unconditional stability the GBDF-B scheme tends to be less dissipative with (θ_1,θ_2) values falling on the left boundary, $\theta_1 = 1/2$.

Plots of the spectral radius $\rho_{\mathbf{G}}$ as a function of $\Delta t/T$ for several (θ_1,θ_2) values lying on the left boundary of the domain of unconditional stability have been shown in Fig. 5(a). In Fig. 5(b) we compare the fraction of energy loss per period as a function of $\Delta t/T$ for the same pairs of (θ_1,θ_2) values. It is evident that for fixed (θ_1,θ_2) values the dissipativity of the GBDF-B scheme increases with increasing time step size $\Delta t/T$. Furthermore it indicates that, along the left boundary $\theta_1 = 1/2$, the dissipativity of the scheme decreases as θ_2 decreases for a fixed time step size. Therefore, the GBDF-B scheme with $(\theta_1,\theta_2) = (1/2, 4/5)$ is the least dissipative member of this family of unconditionally stable algorithms.

The GBDF-B algorithm will be employed to solve the semi-discretized nonlinear elastodynamic equation, with the requirement that the algorithmic parameters (θ_1,θ_2) be located within the domain of unconditional stability. The discretization leads to a system of nonlinear algebraic equations with $\mathbf{U}^{n+1}$ as the unknown, which is solved with a Newton-type

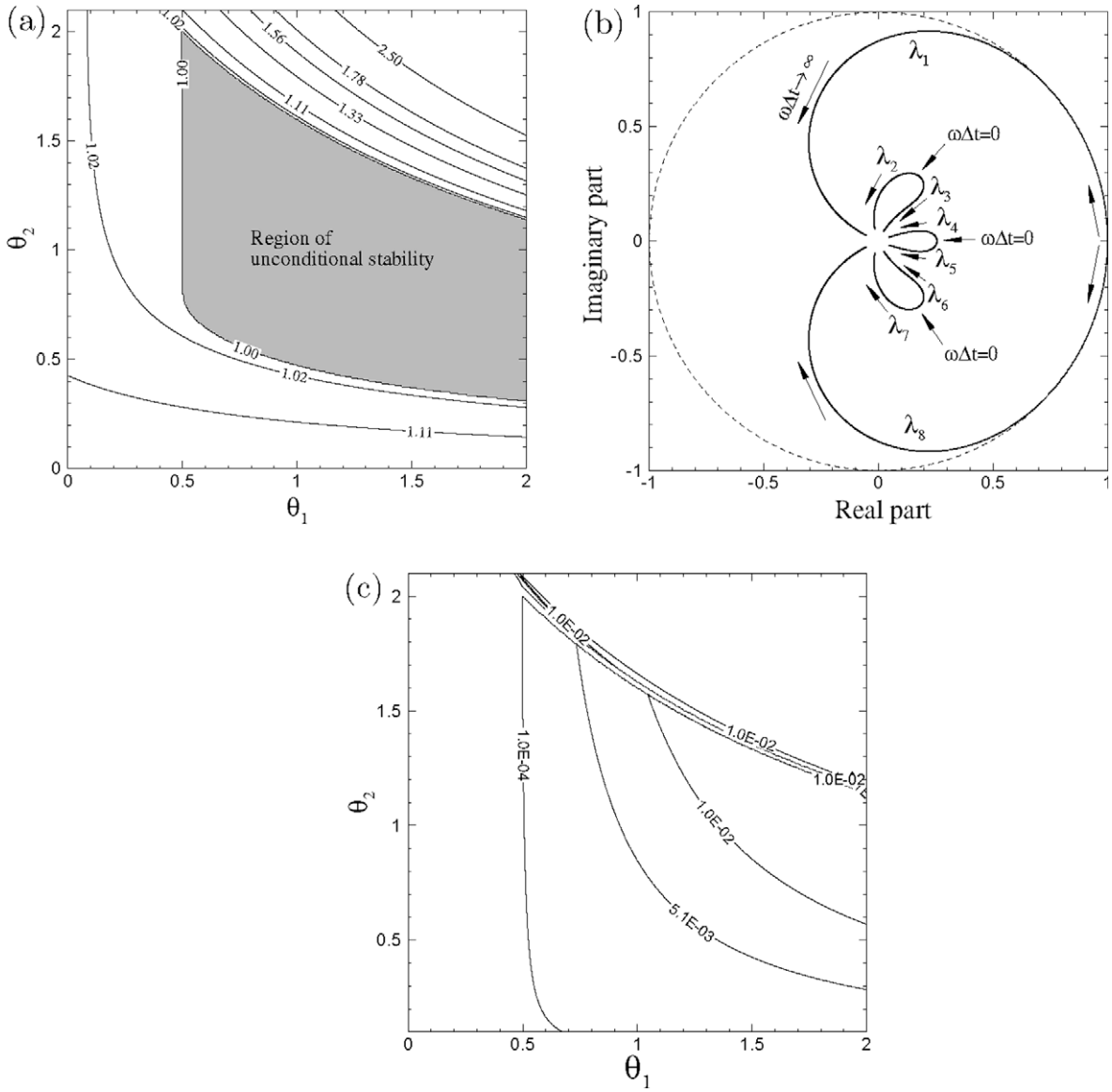

Fig. 4. GBDF-B algorithm: (a) contours in $\theta_1 - \theta_2$ plane of the maximum spectral radius $\rho_{\max}(\theta_1, \theta_2)$ with the linear vibration equation, (b) eigenvalue distribution in the complex plane for $0 \leqslant \omega\Delta t < \infty$ corresponding to $(\theta_1, \theta_2) = (1/2, 4/5)$ and (c) contours of fraction of energy loss per period in $\theta_1 - \theta_2$ plane computed with a fixed time step size $\Delta t/T = 0.02$. T is the period of vibration.

iterative method. Afterwards Eq. (23) can be used to compute $\dot{\mathbf{U}}^{n+1}$ and $\ddot{\mathbf{U}}^{n+1}$. In Section 5 we will present several nonlinear numerical examples computed with this algorithm. Since the scheme requires historical information (step $n-3$), some other algorithm (e.g. trapezoidal rule) needs to be used to calculate the first steps to initiate the computation.

3.2. A composite method based on BDF-like schemes

We next present a composite time integration algorithm incorporating the BDF-like scheme of the previous section and the trapezoidal rule using a strategy similar to [3]. We consider the time step from n to $(n+1)$ consists of two equal sub-steps. In the first sub-step, from n to $(n+1/2)$ (i.e. from t to $t+\Delta t/2$), the trapezoidal rule is employed to solve the semi-discretized elastodynamic equation; In the second sub-step, from $(n+1/2)$ to $(n+1)$ (or from $t+\Delta t/2$ to $t+\Delta t$), the BDF-like algorithm of the previous section is employed for the computation.

More specifically, in the first sub-step we enforce the semi-discretized nonlinear elastodynamic Eq. (7) at time step $(n+1/2)$,

$$\mathbf{M}\ddot{\mathbf{U}}^{n+\frac{1}{2}} + \mathbf{N}^{n+\frac{1}{2}} - \mathbf{R}^{n+\frac{1}{2}} = 0. \tag{25}$$

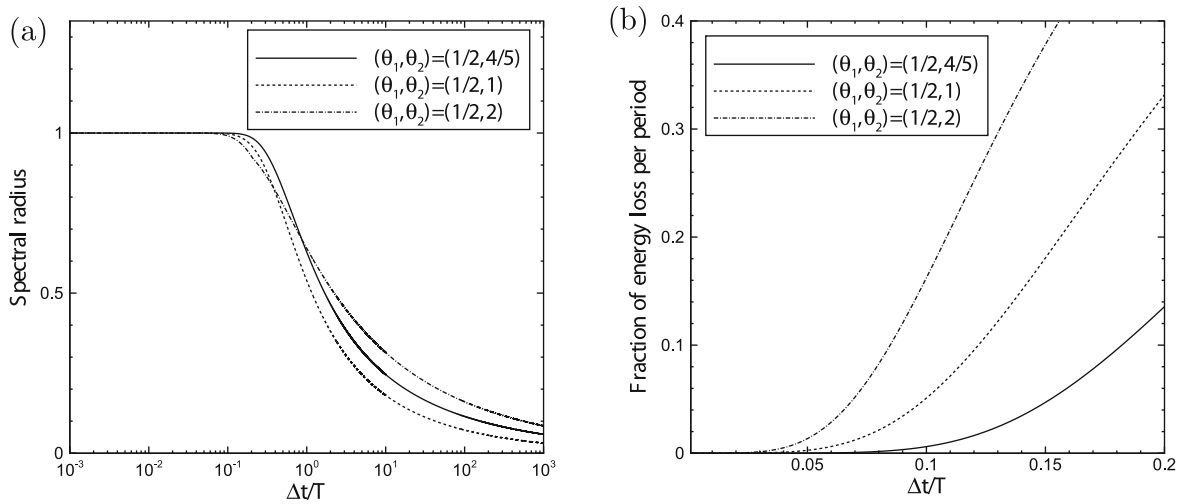

Fig. 5. GBDF-B algorithm: spectral radius (a) and fraction of energy loss per period (b) as a function of $\Delta t/T$ with different (θ_1, θ_2) parameters.

The trapezoidal rule is then used to discretize the above equation,

$$\begin{cases} \mathbf{U}^{n+\frac{1}{2}} = \mathbf{U}^n + \frac{\Delta t}{4}(\dot{\mathbf{U}}^n + \dot{\mathbf{U}}^{n+\frac{1}{2}}) \\ \dot{\mathbf{U}}^{n+\frac{1}{2}} = \dot{\mathbf{U}}^n + \frac{\Delta t}{4}(\ddot{\mathbf{U}}^n + \ddot{\mathbf{U}}^{n+\frac{1}{2}}). \end{cases} \tag{26}$$

After eliminating $\dot{\mathbf{U}}^{n+\frac{1}{2}}$ from Eq. (26) and substituting $\ddot{\mathbf{U}}^{n+\frac{1}{2}}$ into Eq. (25), one obtains a nonlinear algebraic equation about $\mathbf{U}^{n+\frac{1}{2}}$, which can be solved with a Newton-type method.

For the second sub-step we employ a BDF-like scheme such as the GBDF-B scheme with a time step size $\Delta t/2$.

$$\begin{cases} \dot{\mathbf{U}}^{n+1} = \frac{A_1(\theta_1,\theta_2)}{\Delta t/2}\mathbf{U}^{n+1} + \frac{A_2(\theta_1,\theta_2)}{\Delta t/2}\mathbf{U}^{n+\frac{1}{2}} + \frac{A_3(\theta_1,\theta_2)}{\Delta t/2}\mathbf{U}^{n} + \frac{A_4(\theta_1,\theta_2)}{\Delta t/2}\mathbf{U}^{n-\frac{1}{2}} + \frac{A_5(\theta_1,\theta_2)}{\Delta t/2}\mathbf{U}^{n-1} \\ \ddot{\mathbf{U}}^{n+1} = \frac{A_1(\theta_1,\theta_2)}{\Delta t/2}\dot{\mathbf{U}}^{n+1} + \frac{A_2(\theta_1,\theta_2)}{\Delta t/2}\dot{\mathbf{U}}^{n+\frac{1}{2}} + \frac{A_3(\theta_1,\theta_2)}{\Delta t/2}\dot{\mathbf{U}}^{n} + \frac{A_4(\theta_1,\theta_2)}{\Delta t/2}\dot{\mathbf{U}}^{n-\frac{1}{2}} + \frac{A_5(\theta_1,\theta_2)}{\Delta t/2}\dot{\mathbf{U}}^{n-1} \end{cases} \tag{27}$$

Eliminating $\dot{\mathbf{U}}^{n+1}$ from Eq. (27) and substituting $\ddot{\mathbf{U}}^{n+1}$ into Eq. (8) result in a nonlinear algebraic equation about $\mathbf{U}^{n+1}$, which can be solved with a Newton method. The above composite scheme will be referred to as the GBDF-TR algorithm hereafter.

The zero-stability requirement for the GBDF-TR composite scheme yields the following conditions on the parameters (θ_1, θ_2):

$$\left(\theta_1 + \frac{3}{2}\right)\theta_2 < \frac{19}{4}, \quad \theta_2 \geqslant -2 \tag{28}$$

or

$$\left(\theta_1 + \frac{3}{2}\right)\theta_2 > \frac{19}{4}, \quad \theta_2 \leqslant -2. \tag{29}$$

In order to determine the range of (θ_1, θ_2) values for the GBDF-TR scheme, we again employ the spectral analysis using Eq. (16). Applying the GBDF-TR composite scheme to this equation leads to the following iterative relation:

$$[u^{n+1}\ u^{n+\frac{1}{2}}\ u^n\ \dot{u}^{n+1}\ \dot{u}^{n+\frac{1}{2}}\ \dot{u}^n\ \ddot{u}^{n+1}]^T = \mathbf{G}[u^n\ u^{n-\frac{1}{2}}\ u^{n-1}\ \dot{u}^n\ \dot{u}^{n-\frac{1}{2}}\ \dot{u}^{n-1}\ \ddot{u}^n]^T, \tag{30}$$

where $\mathbf{G}$ is the amplification matrix and its specific form is provided in Appendix A.

Fig. 6(a) shows contours of the maximum spectral radius, $\rho_{\max}(\theta_1, \theta_2) = \max_{0 \leqslant \frac{\Delta t}{T} < \infty} \rho_{\mathbf{G}}(\theta_1, \theta_2, \omega\Delta t)$, in the $\theta_1 - \theta_2$ plane, where $\rho_{\mathbf{G}}(\theta_1, \theta_2, \omega\Delta t)$ is the spectral radius of the amplification matrix.

Within the shaded region (which excludes the boundary curve on the top side) $\rho_{\max}$ has an identical unit value. A typical distribution of eigenvalues of the amplification matrix in the complex plane for (θ_1, θ_2) parameters from the shaded region is shown in Fig. 6(b), which corresponds to $(\theta_1, \theta_2) = (7/9, 9/10)$. One can observe that the amplification matrix has no repeated eigenvalue with a unit norm for any $\omega\Delta t > 0$. This observation also applies to other (θ_1, θ_2) values from the shaded region. The GBDF-TR algorithm is therefore linearly unconditionally stable for (θ_1, θ_2) parameters located in the shaded region of Fig. 6(a). Note that the parameter values of (θ_1, θ_2) within this region also satisfy the zero-stability condition (Eq. (28)). We have also studied the GBDF-TR algorithm for the damped vibration Eq. (18) and confirmed its unconditional stability in the presence of physical damping with (θ_1, θ_2) values located in the shaded region of Fig. 6(a).

Fig. 6(c) shows contours of the fraction of energy loss per period in the $\theta_1 - \theta_2$ plane, computed using a fixed time step size $\Delta t/T = 0.02$. It indicates that, within the domain of unconditional stability, the GBDF-TR schemes with (θ_1, θ_2) values

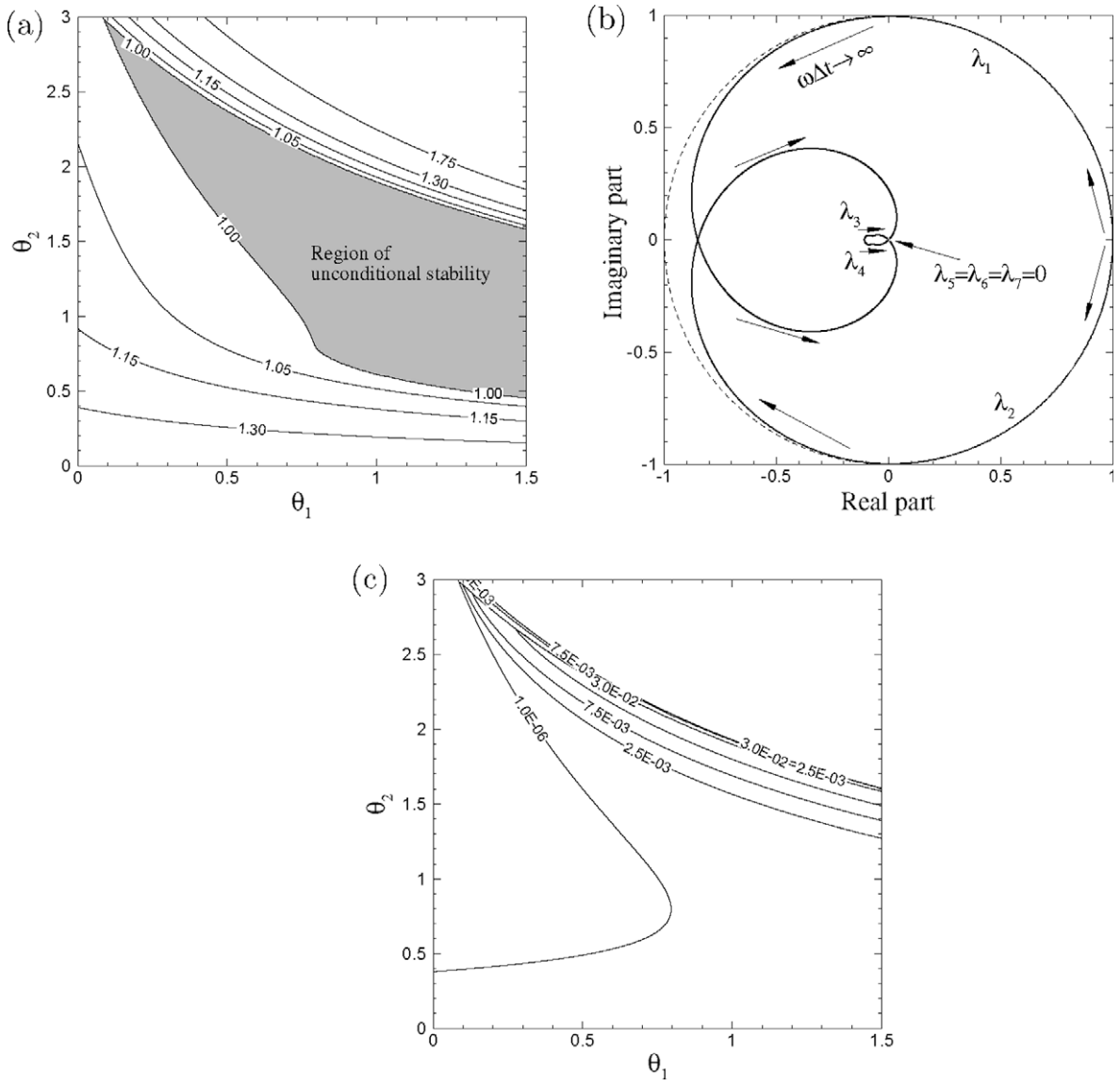

Fig. 6. GBDF-TR algorithm: contours in $\theta_1 - \theta_2$ plane of (a) the maximum spectral radius $\rho_{\max}(\theta_1, \theta_2)$, and (c) the fraction of energy loss per period (with $\Delta t/T = 0.02$) and (b) distribution of eigenvalues of amplification matrix for $0 \leqslant \omega\Delta t < \infty$ with $(\theta_1, \theta_2) = (7/9, 9/10)$.

lying on the boundary curve on the left side are generally associated with low dissipativity. The spectral radii as a function of $\Delta t/T$ for several (θ_1, θ_2) values lying on this boundary curve have been shown in Fig. 7(a). Fig. 7(b) shows the fraction of energy loss as a function of $\Delta t/T$ for the same set of (θ_1, θ_2) values. We observe that the GBDF-TR scheme becomes more dissipative as the time step size $\Delta t/T$ increases, similar to the BDF-like schemes, and that along the left boundary of the domain of unconditional stability the scheme becomes more dissipative as θ_2 increases.

3.3. An extension of the Bathe composite strategy

In this section we present an algorithm that can be regarded as an extension of the Bathe composite strategy [3]. This algorithm retains the self-starting nature and second-order temporal accuracy of the Bathe method, but improves upon the dissipativity. We borrow the idea from [3] that a time step of size Δt is treated as two equal sub-steps of size $\Delta t/2$. In the first sub-step, from n to $(n + 1/2)$ Eq. (7) is enforced at $n + 1/2$ (Eq. (25)). The unknowns to solve are the displacement $\mathbf{U}^{n+\frac{1}{2}}$, velocity $\dot{\mathbf{U}}^{n+\frac{1}{2}}$, and acceleration $\ddot{\mathbf{U}}^{n+\frac{1}{2}}$.

To solve this sub-step we employ a variant form of the Newmark-(β, γ) scheme with $\gamma = 1/2$, represented by the following equations,

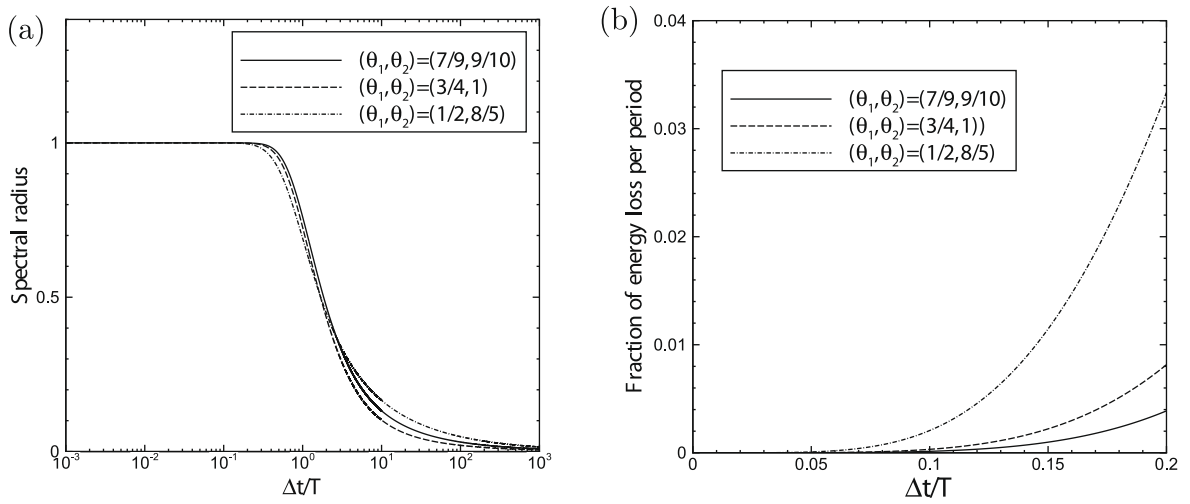

Fig. 7. GBDF-TR algorithm: spectral radius (a) and fraction of energy loss per period (b) as a function of $\Delta t/T$ for different (θ_1, θ_2) parameters.

$$\theta_2 \mathbf{U}^{n+\frac{1}{2}} - \theta_2 \mathbf{U}^n = \theta_2 \left(\frac{\Delta t}{2}\right) \dot{\mathbf{U}}^n + \left(\frac{\Delta t}{2}\right)^2 \ddot{\mathbf{U}}^{n+\frac{1}{2}} + \left(\frac{\theta_2}{2} - 1\right) \left(\frac{\Delta t}{2}\right)^2 \ddot{\mathbf{U}}^n, \tag{31}$$

$$\mathbf{U}^{n+\frac{1}{2}} - \mathbf{U}^n = \frac{\Delta t}{4} \left(\dot{\mathbf{U}}^{n+\frac{1}{2}} + \dot{\mathbf{U}}^n\right), \tag{32}$$

where the algorithmic parameter $\theta_2 (\theta_2 \neq 0)$ plays the role of $1/\beta$, and $\theta_2 = 4$ corresponds to the trapezoidal rule. The above formulas are second-order accurate for any non-zero value of θ_2, as is well-known. Note that if this scheme alone is employed to solve the linear elastodynamic equation, the condition $0 < \theta_2 \leqslant 4$ is required for stability.

In the second sub-step, from $(n + 1/2)$ to $(n + 1)$, the semi-discretized Eq. (7) is enforced at time $t + \Delta t$ (Eq. (8)). The unknowns to solve are the displacement $\mathbf{U}^{n+1}$, velocity $\dot{\mathbf{U}}^{n+1}$, and acceleration $\ddot{\mathbf{U}}^{n+1}$ at step $(n + 1)$. We employ the following scheme to solve this sub-step,

$$\left(3 - \frac{3}{2}\theta_1\right) \mathbf{U}^{n+1} - 6(1 - \theta_1) \mathbf{U}^{n+\frac{1}{2}} + \left(3 - \frac{9}{2}\theta_1\right) \mathbf{U}^n = 2 \left(\frac{\Delta t}{2}\right) \dot{\mathbf{U}}^{n+\frac{1}{2}} + (3\theta_1 - 2) \left(\frac{\Delta t}{2}\right) \dot{\mathbf{U}}^n + \left(\frac{\Delta t}{2}\right)^2 \ddot{\mathbf{U}}^{n+1}, \tag{33}$$

$$\frac{3}{2} \mathbf{U}^{n+1} - 2\mathbf{U}^{n+\frac{1}{2}} + \frac{1}{2} \mathbf{U}^n = \frac{\Delta t}{2} \dot{\mathbf{U}}^{n+1}, \tag{34}$$

where θ_1 is an algorithmic parameter $(\theta_1 \neq 2)$, and $\mathbf{U}^{n+\frac{1}{2}}$ and $\dot{\mathbf{U}}^{n+\frac{1}{2}}$ are known from the first sub-step. It can be verified through Taylor expansions that Eq. (33) represents a second-order accurate relation for any value of θ_1. Note that the above scheme with $\theta_1 = 1/2$ is equivalent to, but has a different formulation than, the second-order backward Euler method applied to both $\dot{\mathbf{U}}^{n+1}$ and $\ddot{\mathbf{U}}^{n+1}$.

The algorithm represented by Eqs. (31)–(34) is a family of second-order composite schemes with θ_1 and $\theta_2 (\theta_1 \neq 2$ and $\theta_2 \neq 0)$ as algorithmic parameters. We will subsequently refer to this algorithm as the SDMM-Newmark composite scheme.

We next determine the range of the parameter values based on Eq. (16). Note that this composite scheme *as a whole* is zero-stable (i.e. stable as $\Delta t \to 0$) for any (θ_1, θ_2) value with $\theta_1 \neq 2$ and $\theta_2 \neq 0$, even though the individual algorithm of the second sub-step represented by Eqs. (33) and (34) is only zero-stable under the condition $0 < \theta_1 \leqslant 1$.

Employing this scheme to discretize Eq. (16) and advance from time step n to $(n + 1)$, one obtains the following iterative relation:

$$[u^{n+1} \ \dot{u}^{n+1} \ \ddot{u}^{n+1}]^T = \mathbf{G} [u^n \ \dot{u}^n \ \ddot{u}^n]^T. \tag{35}$$

The form of the amplification matrix $\mathbf{G}$ is provided in Appendix A.

Fig. 8(a) shows contours in the $\theta_1 - \theta_2$ plane of the maximum spectral radius, $\rho_{\max}(\theta_1, \theta_2) = \max_{0 \leqslant \omega \Delta t < \infty} \rho_{\mathbf{G}}(\theta_1, \theta_2, \omega \Delta t)$. The shaded region in the plot marks the domain in which $\rho_{\max}$ has an identical unit value. On the right and the bottom sides this domain is bounded by the lines $\theta_1 = 2$ and $\theta_2 = 0$ (excluding these lines), respectively; The tip of the domain on the left side corresponds to the point $(\theta_1, \theta_2) = (0, 3)$.

With (θ_1, θ_2) parameters located in the shaded region, the amplification matrix has no repeated eigenvalue with a unit norm for all $\omega \Delta t > 0$. This is illustrated in Fig. 8(b) with the eigenvalue distribution (for $0 \leqslant \omega \Delta t < \infty$) in the complex plane corresponding to $(\theta_1, \theta_2) = (7/10, 16/3)$. One can observe a pair of complex conjugate eigenvalues (λ_1 and λ_2) which becomes distinct real eigenvalues for a range of moderate $\omega \Delta t$ values, and a third eigenvalue (λ_3) which is identically zero. For all

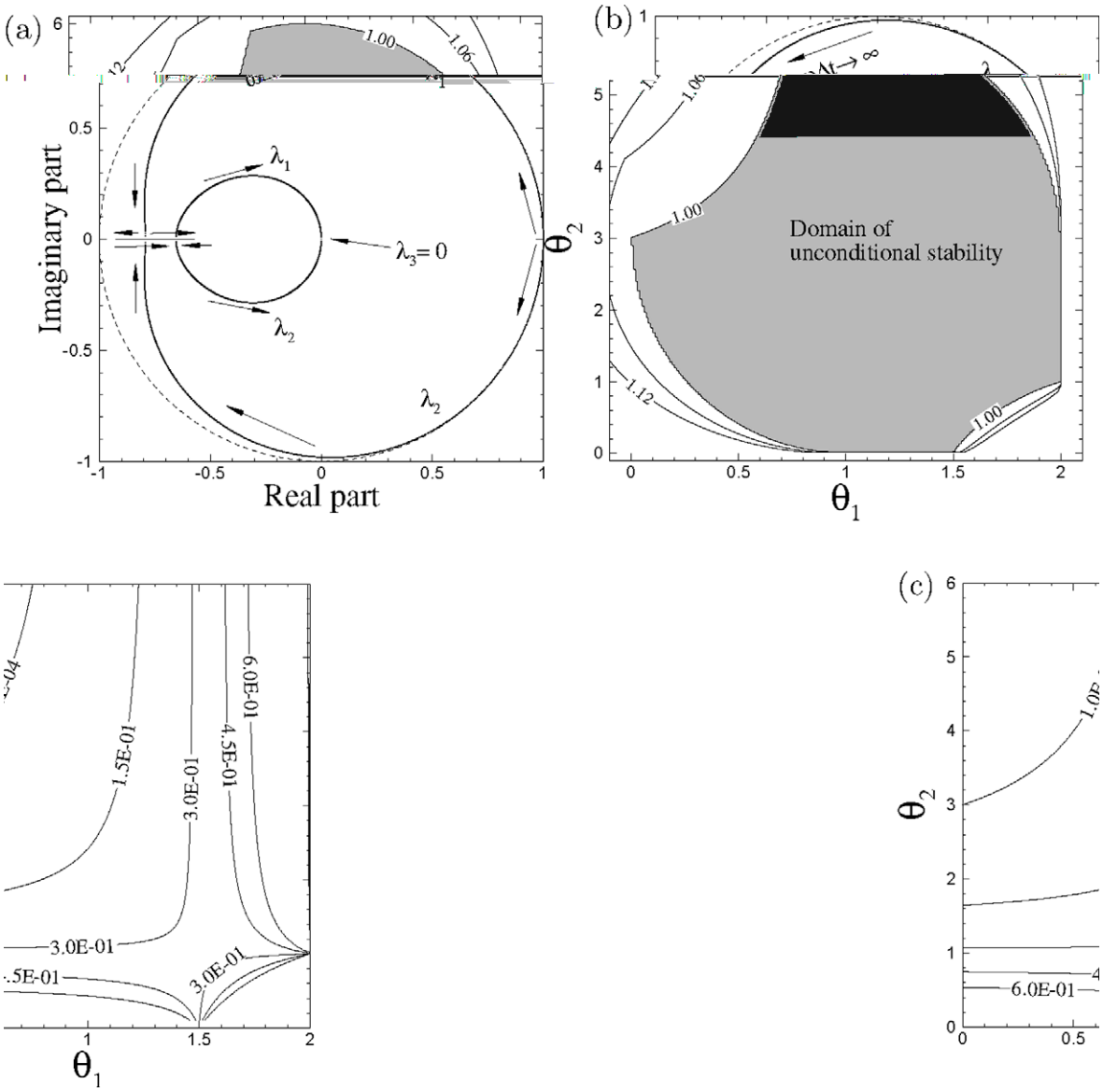

Fig. 8. SDMM-Newmark algorithm: contours in $\theta_1 - \theta_2$ plane of (a) the maximum spectral radius $\rho_{\max}(\theta_1, \theta_2)$, and (c) the fraction of energy loss per period (computed with time step size $\Delta t/T = 0.02$) and (b) distribution of eigenvalues of the amplification matrix for $0 \leqslant \omega\Delta t < \infty$ corresponding to $(\theta_1, \theta_2) = (7/10, 16/3)$; arrows near each curve indicate how the eigenvalues evolve as $\omega\Delta t$ increases.

$\omega\Delta t > 0$ no eigenvalue of the amplification matrix is repeated with a unit norm. This observation also applies to other (θ_1, θ_2) values from the shaded region. Therefore, the shaded region of Fig. 8(a) corresponds to the domain of unconditional stability of the SDMM-Newmark algorithm.

In the presence of physical damping the SDMM-Newmark algorithm with (θ_1, θ_2) from this domain is also unconditionally stable.

Fig. 8(c) shows contours in the $\theta_1 - \theta_2$ plane of the energy loss fraction for a fixed time step size $\Delta t/T = 0.02$. The distribution shows that in the region $\theta_1 < 3/2$ the dissipativity increases as θ_2 decreases for a fixed θ_1 value, and that in the region $\theta_2 > 1$ the dissipativity increases as θ_1 increases for a fixed θ_2 value. Comparison between Fig. 8(a) and (c) indicates that within the domain of unconditional stability the (θ_1, θ_2) values lying on the boundary curve on the left-top side $(0 \leqslant \theta_1 \lesssim 0.742, 3 \leqslant \theta_2 \lesssim 5.9)$ are associated with the lowest dissipativity within this family of algorithms; The (θ_1, θ_2) values lying on the bottom-right boundary curve of this domain $(1.5 < \theta_1 < 2, 0 < \theta_2 < 1)$ are also associated with relatively low dissipativity, but they are more dissipative than those on the left-top boundary curve.

Fig. 9(a) shows the spectral radii as a function of time step size $\Delta t/T$ for several (θ_1, θ_2) values lying on the left-top boundary curve of the domain of unconditional stability. The "hunch" on the curves around $\Delta t/T \approx 0.83$ corresponds to the

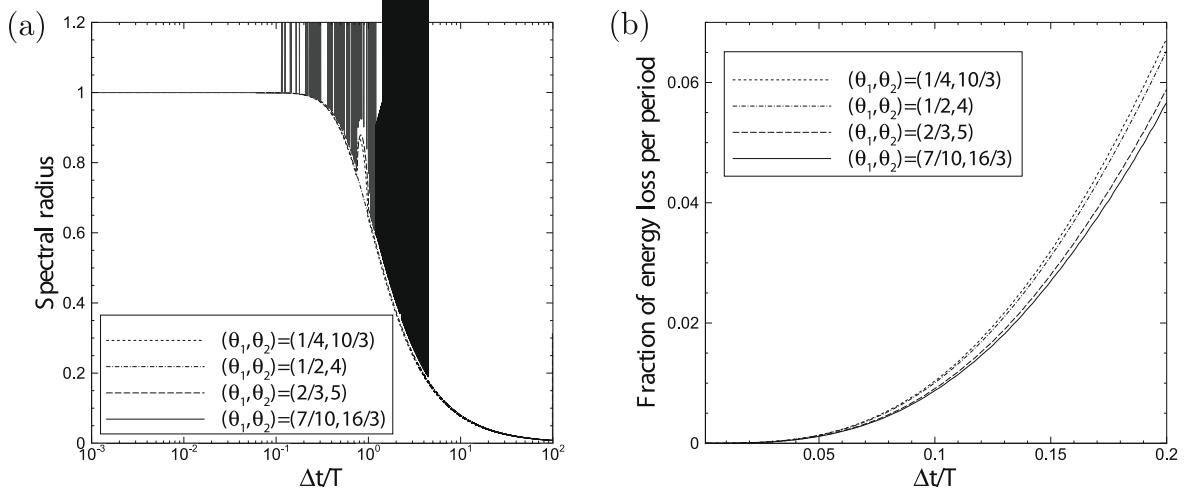

Fig. 9. SDMM-Newmark algorithm: spectral radius (a) and the fraction of energy loss per period (b) as a function of time step size $\Delta t/T$ for several (θ_1, θ_2) values.

situation where all three eigenvalues of the amplification matrix are real and distinct at those time step size values; This is the case for the (θ_1, θ_2) values residing on the left-top boundary curve except for the point $(\theta_1, \theta_2) = (1/2, 4)$, which corresponds to the Bathe method. In Fig. 9(b) we compare the fraction of energy loss as a function of $\Delta t/T$ for the same set of (θ_1, θ_2) values. It indicates that along the left-top boundary curve the dissipativity of the algorithm decreases as θ_2 increases.

The family of composite algorithms, represented by Eqs. (31)–(34), with the (θ_1, θ_2) parameter values residing in the domain of unconditional stability (Fig. 8) will be employed to solve the nonlinear elastodynamic equation. The members with (θ_1, θ_2) values lying on the top-left boundary curve of this domain are preferred, while the rest of the family are very dissipative.

These composite algorithms are self-starting, similar to the Bathe method. We will demonstrate the numerical performance of these schemes with nonlinear examples in Section 5.

4. Convergence characteristics

The goal of this section is to numerically demonstrate the convergence characteristics of the time integration schemes presented in the previous section. We consider the nonlinear vibration, with finite deformation throughout time, of a cubic object of a compressible Neo-Hookean material, whose motion is described by an analytic solution to the nonlinear elastodynamic equation.

Specifically, we consider the cubic block depicted in Fig. 10, which initially occupies the domain $\{(X, Y, Z) \mid 0 \leqslant X \leqslant 1,\ 0 \leqslant Y \leqslant 1,\ 0 \leqslant Z \leqslant 1\}$ in its undeformed configuration. The block is assumed to be Neo-Hookean, characterized by Eq. (4) with material constants μ and λ. The density of the block in its natural configuration is denoted by ρ_0.

The setting of the problem is as follows. The face $X = 0$ is clamped throughout time. On the rest of the faces a time-dependent traction force field, $\mathbf{T} = (T_X, T_Y, T_Z)$, as specified below has been applied,

$$\begin{cases} T_X = n_X[\mu(J_a - 1/J_a) + \lambda \log J_a/J_a] \\ T_Y = n_Y \log J_a \\ T_Z = n_Z \log J_a. \end{cases} \tag{36}$$

In the above equation, $\mathbf{n} = (n_X, n_Y, n_Z)$ denotes the outward-pointing unit vector normal to the surface. The function J_a is given by, $J_a = A + B\sin(at) + Cb\cos(bX)$, where A, B, C, a and b are prescribed constants. The object experiences an external time-dependent body force field, $\rho_0\mathbf{f} = (f_X, f_Y, f_Z)$, as specified below,

$$\begin{cases} f_X = -Ba^2X\sin(at) + [\mu(1 + 1/J_a^2) + \lambda(1 - \log J_a)/J_a^2]Cb^2\sin(bX)/\rho_0 \\ f_Y = 0 \\ f_Z = 0. \end{cases} \tag{37}$$

The initial displacements (u_X, u_Y, u_Z) and initial velocity $(\dot{u}_X, \dot{u}_Y, \dot{u}_Z)$ are provided,

$$\begin{cases} u_X = (A - 1)X + C\sin(bX), \quad u_Y = u_Z = 0, \\ \dot{u}_X = BaX, \quad \dot{u}_Y = \dot{u}_Z = 0. \end{cases} \tag{38}$$

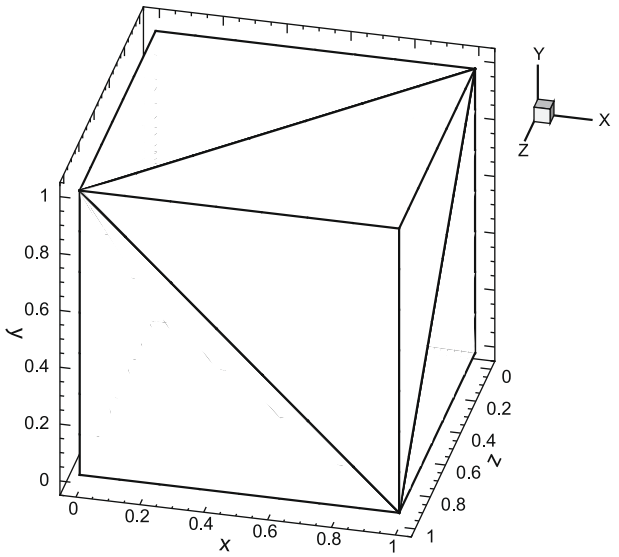

Fig. 10. Neo-Hookean cubic block in nonlinear vibration, discretized with 5 tetrahedral elements.

With these conditions, the problem has the following analytic solution for the displacements with respect to the coordinates of the initial configuration:

$$\begin{cases} u_X = [A - 1 + B\sin(at)]X + C\sin(bX) \\ u_Y = 0 \\ u_Z = 0. \end{cases} \tag{39}$$

It is straightforward to verify that the solution described by Eq. (39), together with the body force in Eq. (37) and the traction force in Eq. (36), satisfies the nonlinear elastodynamic Eq. (1) for a compressible Neo-Hookean material described by Eq. (4).

To simulate the nonlinear vibration of the object numerically, we discretize the cubic domain with five tetrahedral elements (see Fig. 10). We employ a high-order spectral element method [15] for spatial discretizations of the nonlinear momentum Eq. (1). For temporal discretization we employ the time integration schemes presented in the previous section. Dirichlet boundary condition with zero displacement is imposed on the face $X = 0$, and traction boundary conditions based on Eq. (36) are imposed on the other faces. The initial conditions for the displacement and velocity are set according to Eq. (38).

To investigate the temporal convergence of these algorithms, we use a fixed element order (i.e. order of highest expansion polynomial in shape functions) and vary the time step size Δt systematically. For each time step size we integrate the momentum equation over time from $t = 0$ to $t = t_f$, and then compute the L^∞, L^2 and H^1 errors of the displacement fields at $t = t_f$ against the analytic solution (Eq. (39)).

The temporal convergence characteristics of the proposed algorithms are shown in Fig. 11, in which we plot the L^∞, L^2 and H^1 errors of the three displacement fields as a function of the time step size. Fig. 11(a) shows various errors versus Δt computed with the GBDF-B scheme $\theta_1 = 1/2, \theta_2 = 4/5$. Fig. 11(b) shows the H^1 error of the x-displacement field versus Δt computed with various time integration methods, including the trapezoidal rule, GBDF-A ($\theta_1 = 1, \theta_2 = 0$), GBDF-B ($\theta_1 = 1/2, \theta_2 = 4/5$), GBDF-TR scheme ($\theta_1 = 7/9, \theta_2 = 9/10$), and SDMM-Newmark composite scheme ($\theta_1 = 7/10, \theta_2 = 16/3$). The results are obtained employing a fixed element order 4 for all five elements, and the problem is with the following parameter values:

$$\lambda = 20, \quad \mu = 10, \quad \rho_0 = 1.0, \quad A = 1.2, \quad B = 0.2, \quad C = 0.1, \quad a = 1.0, \quad b = 0.01, \quad t_f = 0.2.$$

Note that we have omitted the physical units for all the parameters in this problem as well as in all the numerical examples in subsequent sections. Throughout the paper we will assume that a consistent system of physical units have been employed for the variables and parameters in all the test problems.

It is evident that as the time step size is reduced by half the numerical errors are reduced by a factor of four. These results demonstrate the temporal second-order accuracy of the proposed algorithms in Section 3.

5. Representative numerical examples

To evaluate the performance of the proposed time integration algorithms, we consider several three-dimensional numerical example problems of nonlinear elastodynamics. We solve these problems with the proposed algorithms in Section 3, and compare the results with those from the trapezoidal rule, the Bathe method [3], and the Park method [32]. The test problems

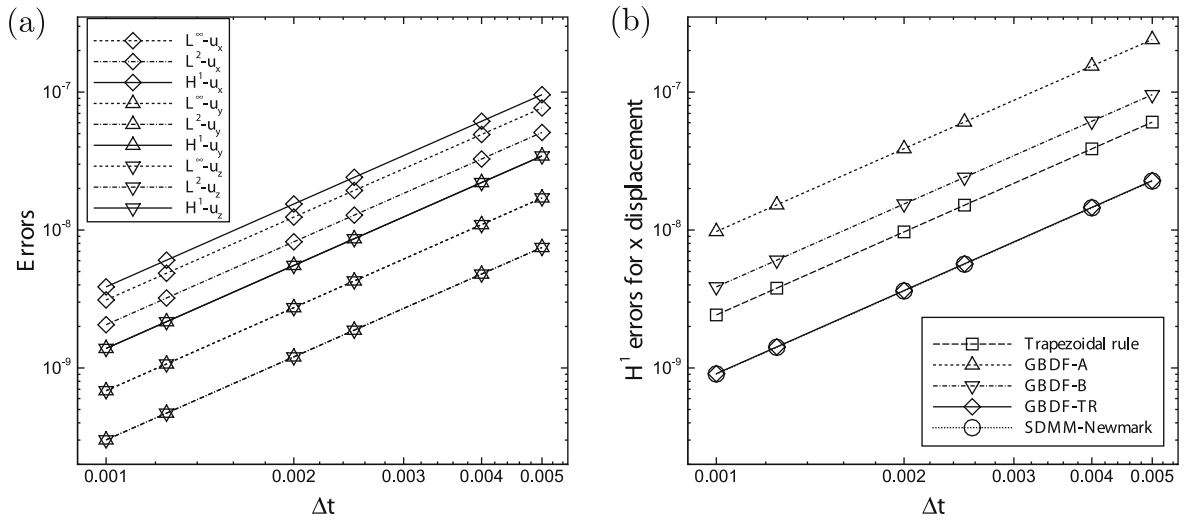

Fig. 11. Temporal second-order accuracy: (a) L^∞, L^2 and H^1 errors of displacements versus Δt computed with the GBDF-B ($\theta_1 = 1/2, \theta_2 = 4/5$) algorithm, (b) H^1 errors of the x displacement versus Δt computed with various methods, for the nonlinear vibration of a Neo-Hookean cubic block. GBDF-A, $(\theta_1, \theta_2) = (1, 0)$; GBDF-B: $(\theta_1, \theta_2) = (1/2, 4/5)$; GBDF-TR: $(\theta_1, \theta_2) = (7/9, 9/10)$; SDMM-Newmark: $(\theta_1, \theta_2) = (7/10, 16/3)$.

involve large deformations, large displacements and rotations, which demonstrate the difficulties encountered by some algorithms. The material models considered are assumed to be of St. Venant-Kirchhoff or compressible Neo-Hookean types, respectively described by Eqs. (2) and (4). As noted in Section 4, the units of physical variables and parameters are omitted with the assumption that a consistent system of units are used for each problem.

The tests involve the free flight of a 3D L-shaped block. This problem has been considered previously by other researchers (see e.g. [36]). Fig. 12 shows the initial undeformed configuration of the block, and provides all values of the geometric dimensions. The origin of the coordinate system is located at the corner vertex that is blocked from view in the figure, and the three axises are along the edges of the block. Two time-dependent traction forces are applied on the two end faces of the block, as marked in Fig. 12. These forces are specified by the following functional forms:

$$\mathbf{F}_1(t) = -\mathbf{F}_2(t) = (150, 300, 450)p(t), \quad p(t) = \begin{cases} t, & 0 \leqslant t < 2.5, \\ 5 - t, & 2.5 \leqslant t < 5, \\ 0, & t \geqslant 5. \end{cases} \tag{40}$$

There is no body force acting on the object. The density of the block in the undeformed configuration is chosen to be $\rho_0 = 1000$. The block is at rest in its undeformed configuration at $t = 0$.

Both St. Venant-Kirchhoff and compressible Neo-Hookean material models are considered for the L-shaped block. With the St. Venant-Kirchhoff model we further consider two cases: a rigid block and a deformable block, implemented, respectively by employing fairly large and small Young's modulus values. Corresponding to these cases, significant or virtually no deformations are involved during the free motion of the block.

Because the net external force acting on the block is zero, the object will simply tumble in space with no net displacement of its center of mass. In order to simulate its motion, we discretize the domain occupied by the block with four hexahedral elements as shown in Fig. 12, in which solid lines mark the edges of the elements. High-order spectral element expansions are employed for spatial discretizations, as outlined in Section 2 and detailed in [15]. An element order of 3 has been employed for all elements in the spatial discretization. Traction boundary conditions according to Eq. (40) are imposed on the end faces of the block where the external forces are applied, while traction-free boundary conditions are employed on the other faces. The time integration algorithms presented in Section 3 are employed for temporal discretization. The initial displacements and initial velocities are set to be zero.

5.1. Rigid L-shaped block

We first investigate the case of a rigid block, implemented with a Young's modulus value $E = 5 \times 10^{10}$, of a St. Venant-Kirchhoff material. The Poisson ratio is $\nu = 0.3$. We have conducted long-time simulations of the object motion (over $t = 1000$) with the proposed algorithms. Let us first investigate the characteristics of the total energy (Eq. (5)). Fig. 13 shows time histories of the total energy of the tumbling block. The four plots correspond to four different time step sizes, ranging from $\Delta t = 0.25$ to $\Delta t = 2.0$. The results in each plot are obtained with the GBDF-A $(\theta_1, \theta_2) = (1, 0)$, GBDF-B $(\theta_1, \theta_2) = (1/2, 4/5)$, GBDF-TR $(\theta_1, \theta_2) = (7/9, 9/10)$, and SDMM-Newmark composite method $(\theta_1, \theta_2) = (7/10, 16/3)$. For each time step size we have also included results computed with the trapezoidal rule, the Bathe method [3], and the Park method [32] for comparison. Simulations

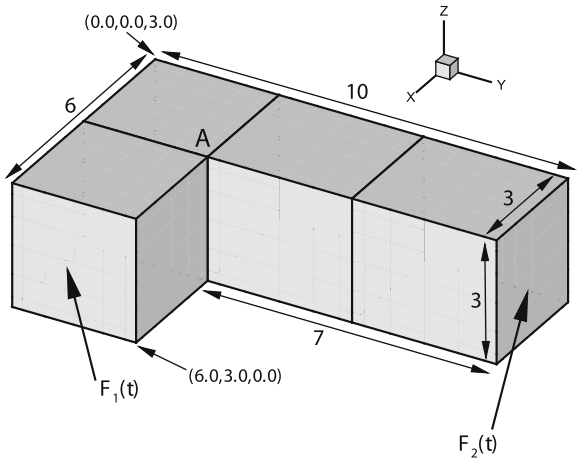

Fig. 12. Undeformed configuration of the L-shaped block.

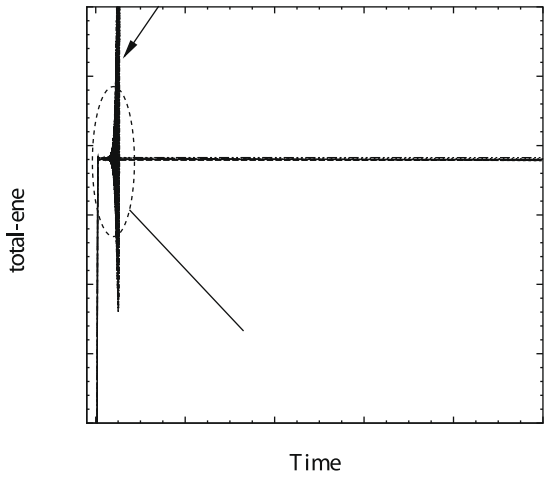

with the trapezoidal rule become unstable in all these cases. Severe fluctuations develop over time in the total energy, which ultimately grows unbounded. With a larger time step size the trapezoidal rule tends to blow up sooner.

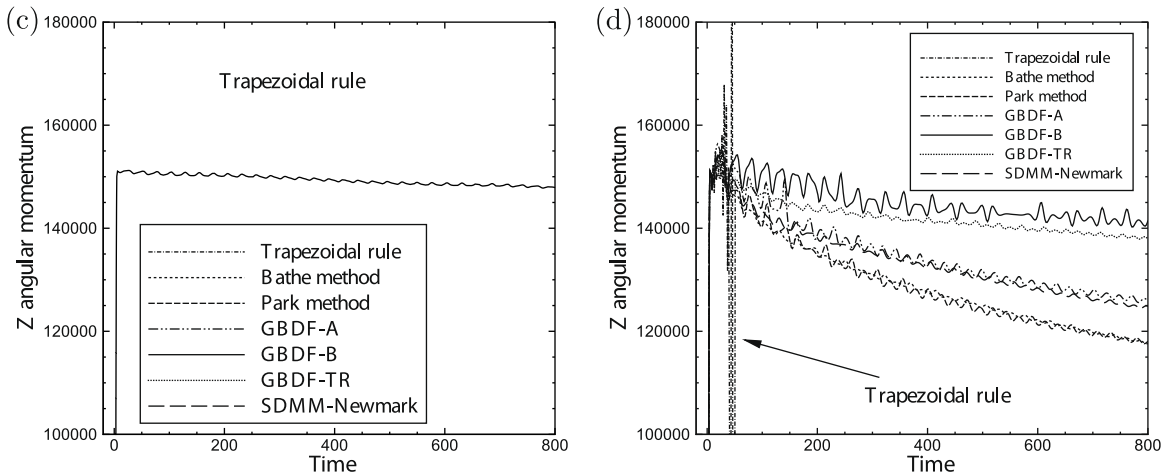

Fig. 14. Free flight of a rigid L-shaped block: time histories of the z-component of the angular momentum computed with $\Delta t = 0.25$ (a), $\Delta t = 0.5$ (b), $\Delta t = 1.0$ (c), and $\Delta t = 2.0$ (d). See caption of Fig. 13 for algorithmic parameter values.

ne
pairs
Fig. 1(a)), $(v_1, v_2) = (1, 0), (1/4, 3/4)$ and (0,1), show only slight
ntly more
ry of the do-
alue inside the
consistent with those from the linear stability analysis in Section 3.

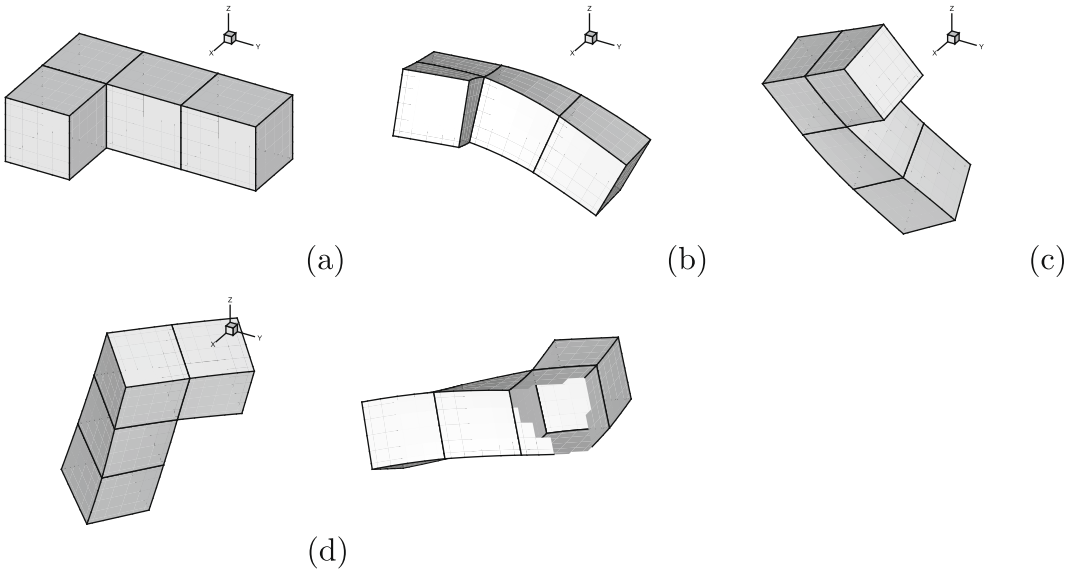

5.2. Deformable L-shaped block

We next study the motion of a soft deformable L-shaped block of the St. Venant-Kirchhoff material, with a Young's modulus $E = 5 \times 10^4$ and a Poisson ratio $\nu = 0.3$. A very long-time history (up to $t > 4000$) of the motion has been simulated. Fig. 16 compares time histories of the total energy computed with different methods, including the proposed schemes d the Bathe and Park methods. The three plots correspond, respectively to time step sizes $\Delta t = 0.2$ (Fig. 16(a)), 0.5 g. 16(b)), and 1.0 (Fig. 16(c)). The Trapezoidal rule is again observed to be unstable in all these cases, exhibiting uncon- led energy growth over time. Stable computations have been achieved with the other methods. In the initial loading stage 0–5) the total energy of the block grows rapidly from zero to about 4.45×10^4. Beyond the initial loading stage all the hods exhibit energy dissipation of the high-frequency modes. With a small time step $\Delta t = 0.2$ (Fig. 16(a)), after the initial l decay all the energy curves appear to gradually level off and settle at certain values over long-time. The long-time en- levels resulting from different methods are comparable to one another, with those from GBDF-B and GBDF-TR slightly r than the rest. The history curves for the GBDF-B and GBDF-TR algorithms essentially overlap with each other over ime. The curves from the Bathe method and the SDMM-Newmark scheme overlap with each other essentially through- e run. As the time step size increases to $\Delta t = 0.5$, the energy histories exhibit similar characteristics to those at 2. But the initial energy decay is faster and the long-time energy levels are generally lower. The long-time energy ed with GBDF-TR stays at a higher level than the other methods, and that from the Park method is slightly lower than

till larger time step $\Delta t = 1.0$, results from different methods exhibit somewhat different characteristics. The energy mputed with both GBDF-B and the GBDF-TR level off over time after the initial rapid decay, with the energy com- ng the GBDF-TR algorithm at a slightly higher level (Fig. 16(c)). In contrast, the history curves computed using the hods show a different character; After the initial rapid energy decrease, the curves do not appear to level off over onsistently decrease albeit at a slower rate.

hows the evolution in time of the angular momentum of the block. Here we have plotted time histories of the z- of the angular momentum computed with different Δt. The angular momentum demonstrates, in a sense, the teristics as the energy. In the initial loading stage the z-component of the angular momentum increases from

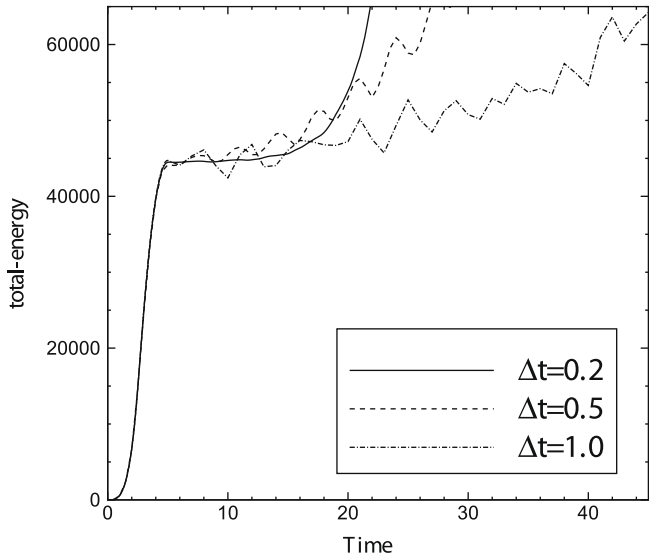

Fig. 19. Free flight of a deformable L-shaped block: time histories of total energy computed using GBDF-B scheme with parameter values *not* in the domain of unconditional stability, $(\theta_1, \theta_2) = (1/2, 1/2)$.

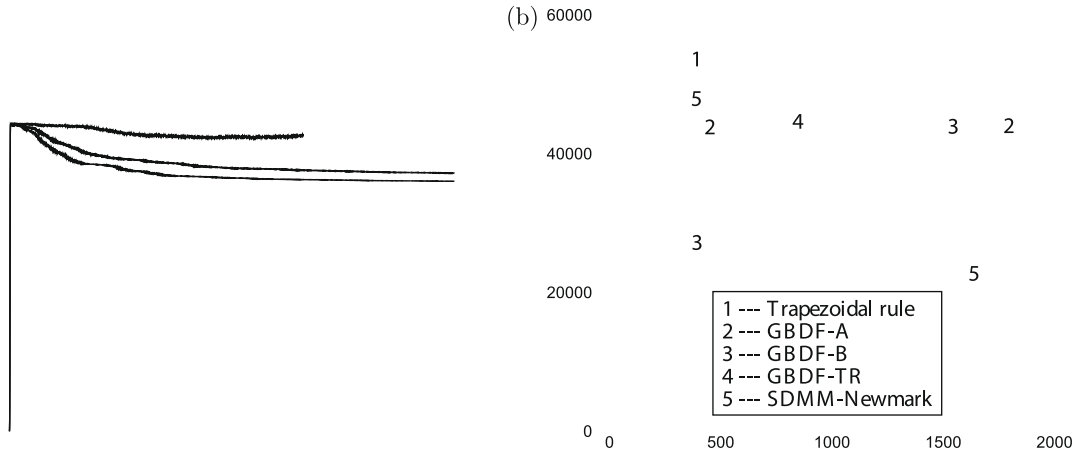

Fig. 20. Free flight of L-shaped block made of a Neo-Hookean material: time histories of the total energy computed with time step sizes $\Delta t = 0.25$ (a) and $\Delta t = 1.0$ (b) using various methods. See caption of Fig. 13 for algorithmic parameters.

1.465×10^5. Note the scale of the vertical axis in these plots; Although the results from different methods show fferent characteristics, their values are actually very close. The instability encountered with the trapezoidal rule ıt from the angular momentum plots. At $\Delta t = 0.2$, the angular momentum from all methods stay essentially at a ·l after slight initial decay. But all the history curves show small-amplitude fluctuations. This suggests that the angular momentum is approximately conserved with these methods, but not exactly at each time step. At $\Delta t = 0.5$, the angular momentum curves computed with all methods except the Bathe method and SDMM-Newmark (excluding trapezoidal rule) level off over time, with some differences in their long-time values. On the other hand, the history curves computed with the Bathe method and the SDMM-Newmark scheme do not appear to level off over time, although the decrease throughout the simulation is quite slight considering the scale of the vertical axis in Fig. 17(b). As the time step size increases to $\Delta t = 1.0$, the angular momentum computed with GBDF-B and GBDF-TR stay at essentially a constant level (with fluctuations) over long-time, while those with the other methods appear to decrease consistently.

These results suggest that the proposed algorithms are quite effective for solving nonlinear elastodynamic problems. Stable computations can be achieved with these methods at large time step sizes where the trapezoidal rule encounters difficulties. The dissipativity of these schemes are influenced by the time step sizes, and increases with increasing time step size.

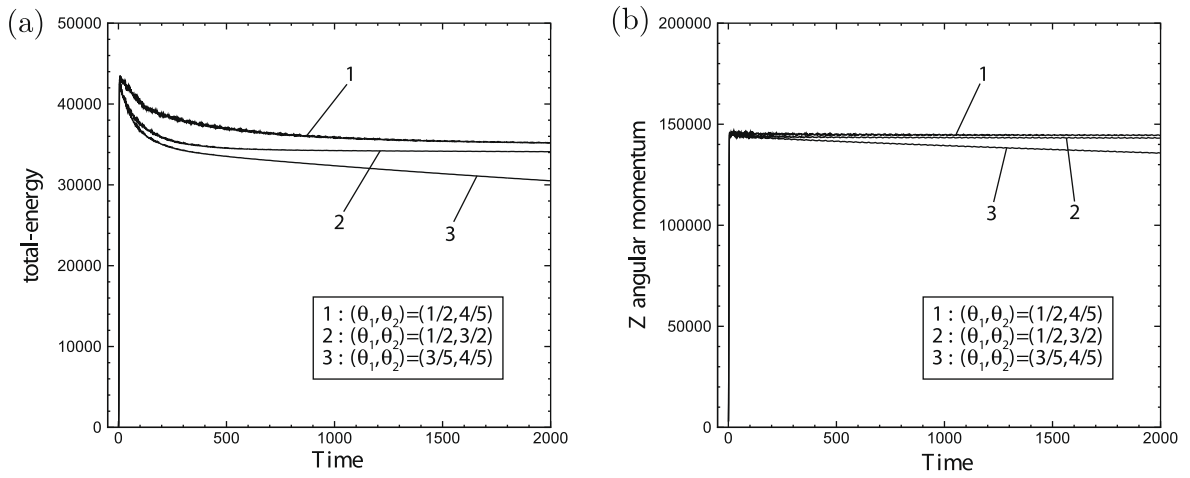

Fig. 22. Free flight of a Neo-Hookean L-shaped block: time histories of total energy (a) and z-component of the angular momentum (b) computed with $\Delta t = 0.5$ using the GBDF-B algorithm with different algorithmic parameters.

approximately at a constant level at small time step sizes, and as the time step size increases the decay in its magnitude appears not very significant, especially with GBDF-B and GBDF-TR.

Fig. 18 shows a temporal sequence of snapshots of the deforming L-shaped block at the initial stages of the simulation. These are obtained using the GBDF-TR scheme with parameters $(\theta_1, \theta_2) = (7/9, 9/10)$ and a time step size $\Delta t = 0.5$. The deformation of the object during the free flight is apparent. In particular, one can observe the twisting and bending of the block, characteristic of the existing high-frequency modes in the short-term solution.

All the results presented so far with the proposed algorithms have been computed using algorithmic parameter values residing within the respective domains of unconditional stability (Section 3). Fig. 19 illustrates the instability that may be encountered if the parameters are *not* within the domain of stability. It shows time histories of the total energy of the deformable L-shaped block computed using the GBDF-B scheme with $(\theta_1, \theta_2) = (1/2, 1/2)$, which is outside of the domain of unconditional stability (see Fig. 4). The time step sizes Δt employed here are the same as those in Fig. 16 considered for the other algorithms. Evidently, the total energy exhibits uncontrolled growth at all three time step sizes, and the computations are unstable.

5.3. L-shaped block of Neo-Hookean material

The tests in the previous two sections involve St. Venant-Kirchhoff materials, we next study the performance of the proposed algorithms for a compressible Neo-Hookean hyperelastic material, using the free flight problem of the 3D L-shaped block. The problem setting has the same geometric parameters and external loading conditions as those in the previous two sections. The Neo-Hookean material is characterized by Eq. (4), and the material parameters $\mu = 1.925 \times 10^4$ and $\lambda = 2.885 \times 10^4$ are assumed in the simulations of this section. The density of the block in the initial undeformed configuration is chosen to be $\rho_0 = 1000$. We simulate the motion of the block using different time step sizes, and monitor the time histories of the total energy and the angular momentum.

Fig. 20 compares time histories of the total energy computed with the four methods discussed in Section 3, together with the trapezoidal rule, for two time step sizes $\Delta t = 0.25$ and $\Delta t = 1.0$. For the $\Delta t = 1.0$ case a smaller time step has been used in the initial loading stage $(0 < t < 5)$ to better resolve the external forces. In the initial loading stage the total energy of the block increases rapidly from zero to about 4.4×10^4. The computation using the trapezoidal rule fails in both cases. The break-down is not due to uncontrolled growth of energy, as observed in previous examples with the St. Venant-Kirchhoff materials, but because the solution yields negative values of the Jacobian (see Eq. (4)), J, at certain points within the domain. As a result, the computation terminates abruptly without showing significant energy growth in the time history. On the other hand, stable solutions have been obtained for long-time simulations (up to $t = 4000$, only the first 2000 time units are shown in Fig. 20 for clarity) using the proposed algorithms. At $\Delta t = 0.25$, with the proposed methods the total energy decays and gradually approaches a constant level over time. The long-time energy level computed using GBDF-TR is higher than those using the other three methods. The energy levels computed with GBDF-B and SDMM-Newmark algorithms are close to each other over time, and are a little higher than that with GBDF-A. At a larger time step size $\Delta t = 1.0$, the energy histories produced by both GBDF-B and GBDF-TR appear to approach a constant level over time after the initial rapid decay. The histories computed using GBDF-A and SDMM-Newmark, on the other hand, appear to decrease consistently at a small rate for their long-term behaviors.

Table 1
Computational cost for the free flight problem of a 3D deformable L-shaped block with different algorithms.

Algorithm	Wall time/step (s)
Trapezoidal rule	0.14–0.34
Bathe method	0.22
GBDF-A	0.12
GBDF-B	0.13
GBDF-TR	0.225
SDMM-Newmark	0.221

The evolution of the angular momentum computed with different methods is compared in Fig. 21. In the plots we show time histories of the angular momentum computed using the proposed algorithms, together with the trapezoidal rule, with a time step size $\Delta t = 1.0$. The magnitude of the angular momenta reaches a value of the order 10^5 at the end of the initial loading stage. Beyond this initial stage, in the absence of external loads we observe that the angular momentum has been approximately conserved, with only very slight decay; It remains at essentially a constant level in the long run. With the trapezoidal rule, after the initial loading vanishes and before the computation fails, we observe that the three components of the angular momentum stay at their respective constant values, with notable fluctuations. With the proposed algorithms, small-amplitude fluctuations can also be observed in the time history, especially at the early stage when the external load is removed. However, overall the angular momentum is approximately at a constant level for all the proposed algorithms.

The results reported above for the Neo-Hookean material are obtained with some specific algorithmic parameter values, namely, GBDF-A $(\theta_1, \theta_2) = (1, 0)$, GBDF-B $(\theta_1, \theta_2) = (1/2, 4/5)$, GBDF-TR $(\theta_1, \theta_2) = (7/9, 9/10)$, and SDMM-Newmark $(\theta_1, \theta_2) = (7/10, 16/3)$. We have also tested other algorithmic parameter values in the domains of stability (Section 3) for different algorithms with this problem, and stable computations have been observed. For example, several tests with the GBDF-B algorithm are illustrated in Fig. 22, in which we plot time histories of the total energy (Fig. 22(a)) and the z-component of the angular momentum (Fig. 22(b)) with several (θ_1, θ_2) values that fall on the boundary of and inside the domain of stability of GBDF-B (Fig. 4). Note that the algorithmic parameter values in these plots are the same as those in Fig. 15(b), which is for a St. Venant-Kirchhoff material.

6. Concluding remarks

In this study we have presented several second-order time integration algorithms based on a BDF-like scheme, together with an extension of the Bathe composite strategy. The domains of appropriate algorithmic parameter values have been determined through a linear stability analysis, and less dissipative members of each algorithm have been identified. We have tested these algorithms with several three-dimensional nonlinear elastodynamic problems. The material models in these tests include St. Venant-Kirchhoff and compressible Neo-Hookean materials, and the problems involve large deformations and displacements, and rotations. Numerical tests with three-dimensional nonlinear problems involving large deformations and rotations and different material models show that the proposed algorithms are quite effective for nonlinear elastodynamics. Stable solutions have been obtained with these algorithms at large time step sizes when the trapezoidal rule encounters a well-known instability.

Among the four algorithms considered here the GBDF-B scheme appears particularly attractive based on these tests and also in terms of computational cost (see below), and is therefore recommended.

Numerical simplicity is one of the notable attributes of these algorithms. They can be implemented in a similar fashion to the trapezoidal rule. They all result in symmetric tangential stiffness matrices for nonlinear problems. These properties are attractive to large-scale nonlinear dynamic analysis of engineering problems.

Although the numerical tests demonstrate the promise of the proposed algorithms, they are no substitute for rigorous theoretical analyses, and the question concerning the stability of these algorithms for general nonlinear elastodynamic problems is open. It would be valuable to perform nonlinear mathematical analyses of these algorithms that prove the numerically observed characteristics. These analyses would also be valuable for further improvement of these algorithms. Such analyses call for much future research and are left for further studies of the algorithms. The multistep nature of these algorithms also leads to the necessity for some startup procedure to initiate the computations.

With regard to the computational cost, in Table 1 we summarize the average wall time per step (in seconds) for the four algorithms presented in Section 3, the trapezoidal rule, and the Bathe method. This is for the free flight problem of a three-dimensional deformable L-shaped block (Section 5.2) with a time step size $\Delta t = 0.5$, computed on a Linux workstation (on a single processor). For the trapezoidal rule, the number of Newton iterations per time step for convergence increases as the simulation proceeds, especially toward the point when it becomes unstable; As a result the wall time per step starts with around 0.14 s and increases to around 0.34 s when the computation becomes unstable. For both GBDF-A and GBDF-B algorithms, the wall time per step decreases slightly as the simulation progresses, with average values of 0.12 and 0.13 s, respectively. The costs of the Bathe method, GBDF-TR and SDMM-Newmark are comparable, with the GBDF-TR slightly larger;

Since they are all composite-type methods requiring an additional solve at $(n+1/2)$, their costs are about twice the cost of GBDF-A and GBDF-B schemes.

Acknowledgment

The author gratefully acknowledges the support from the NSF and the DOE/PSAAP program. Computer time was provided by the TeraGrid through an MRAC grant and by the Rosen Center for Advanced Computing at Purdue University.

Appendix A. Amplification matrices

The amplification matrix $\mathbf{G}$ of the GBDF-A algorithm represented by Eqs. (14) and (15) for the linear vibration Eq. (16) is given by

$$\mathbf{G} = \begin{bmatrix} \mathbf{G}_{11} & \mathbf{G}_{12}\Delta t \\ \mathbf{G}_{21}\frac{1}{\Delta t} & \mathbf{G}_{22} \end{bmatrix}, \tag{41}$$

where

$$\mathbf{G}_{11} = \begin{bmatrix} -\frac{B(\theta_1)A(\theta_2)}{K(\theta_1,\theta_2,\omega\Delta t)} & -\frac{C(\theta_1)A(\theta_2)}{K(\theta_1,\theta_2,\omega\Delta t)} & -\frac{D(\theta_1)A(\theta_2)}{K(\theta_1,\theta_2,\omega\Delta t)} \\ 1 & 0 & 0 \\ 0 & 1 & 0 \end{bmatrix},$$

$$\mathbf{G}_{12} = \begin{bmatrix} -\frac{B(\theta_2)}{K(\theta_1,\theta_2,\omega\Delta t)} & -\frac{C(\theta_2)}{K(\theta_1,\theta_2,\omega\Delta t)} & -\frac{D(\theta_2)}{K(\theta_1,\theta_2,\omega\Delta t)} \\ 0 & 0 & 0 \\ 0 & 0 & 0 \end{bmatrix},$$

$$\mathbf{G}_{21} = \begin{bmatrix} \frac{B(\theta_1)\omega^2\Delta t^2}{K(\theta_1,\theta_2,\omega\Delta t)} & \frac{C(\theta_1)\omega^2\Delta t^2}{K(\theta_1,\theta_2,\omega\Delta t)} & \frac{D(\theta_1)\omega^2\Delta t^2}{K(\theta_1,\theta_2,\omega\Delta t)} \\ 0 & 0 & 0 \\ 0 & 0 & 0 \end{bmatrix},$$

$$\mathbf{G}_{22} = \begin{bmatrix} -\frac{B(\theta_2)A(\theta_1)}{K(\theta_1,\theta_2,\omega\Delta t)} & -\frac{C(\theta_2)A(\theta_1)}{K(\theta_1,\theta_2,\omega\Delta t)} & -\frac{D(\theta_2)A(\theta_1)}{K(\theta_1,\theta_2,\omega\Delta t)} \\ 1 & 0 & 0 \\ 0 & 1 & 0 \end{bmatrix},$$

$$K(\theta_1,\theta_2,\omega\Delta t) = A(\theta_1)A(\theta_2) + \omega^2\Delta t^2.$$

The amplification matrix of the GBDF-B algorithm represented by Eq. (23) is given by

$$\mathbf{G} = \begin{bmatrix} \mathbf{G}_{11} & \mathbf{G}_{12}\Delta t \\ \mathbf{G}_{21}\frac{1}{\Delta t} & \mathbf{G}_{11} \end{bmatrix}, \tag{42}$$

where

$$\mathbf{G}_{11} = \begin{bmatrix} -\frac{A_1(\theta_1,\theta_2)A_2(\theta_1,\theta_2)}{A_1^2(\theta_1,\theta_2)+\omega^2\Delta t^2} & -\frac{A_1(\theta_1,\theta_2)A_3(\theta_1,\theta_2)}{A_1^2(\theta_1,\theta_2)+\omega^2\Delta t^2} & -\frac{A_1(\theta_1,\theta_2)A_4(\theta_1,\theta_2)}{A_1^2(\theta_1,\theta_2)+\omega^2\Delta t^2} & -\frac{A_1(\theta_1,\theta_2)A_5(\theta_1,\theta_2)}{A_1^2(\theta_1,\theta_2)+\omega^2\Delta t^2} \\ 1 & 0 & 0 & 0 \\ 0 & 1 & 0 & 0 \\ 0 & 0 & 1 & 0 \end{bmatrix},$$

$$\mathbf{G}_{12} = \begin{bmatrix} -\frac{A_2(\theta_1,\theta_2)}{A_1^2(\theta_1,\theta_2)+\omega^2\Delta t^2} & -\frac{A_3(\theta_1,\theta_2)}{A_1^2(\theta_1,\theta_2)+\omega^2\Delta t^2} & -\frac{A_4(\theta_1,\theta_2)}{A_1^2(\theta_1,\theta_2)+\omega^2\Delta t^2} & -\frac{A_5(\theta_1,\theta_2)}{A_1^2(\theta_1,\theta_2)+\omega^2\Delta t^2} \\ 0 & 0 & 0 & 0 \\ 0 & 0 & 0 & 0 \\ 0 & 0 & 0 & 0 \end{bmatrix},$$

$$\mathbf{G}_{21} = -\omega^2\Delta t^2\mathbf{G}_{12}.$$

The amplification matrix of the GBDF-TR scheme (Eqs. (26) and (27)) is given by

$$\mathbf{G} = \begin{bmatrix} \mathbf{G}_{11} & \mathbf{G}_{12}\Delta t & \mathbf{G}_{13}\Delta t^2 \\ \mathbf{G}_{21}\frac{1}{\Delta t} & \mathbf{G}_{22} & \mathbf{G}_{23}\Delta t \\ \mathbf{G}_{31}\frac{1}{\Delta t^2} & \mathbf{G}_{32}\frac{1}{\Delta t} & \mathbf{G}_{33} \end{bmatrix}, \tag{43}$$

where

$$\mathbf{G}_{11}=\begin{bmatrix}U_1 & N_3 & N_4\\ L_1 & 0 & 0\\ 1 & 0 & 0\end{bmatrix},\quad \mathbf{G}_{12}=\begin{bmatrix}U_2 & U_3 & U_4\\ L_2 & 0 & 0\\ 0 & 0 & 0\end{bmatrix},\quad \mathbf{G}_{13}=\begin{bmatrix}U_5\\ L_3\\ 0\end{bmatrix},$$
$$\mathbf{G}_{21}=\begin{bmatrix}V_1 & V_2 & V_3\\ M_1 & 0 & 0\\ 0 & 0 & 0\end{bmatrix},\quad \mathbf{G}_{22}=\begin{bmatrix}V_4 & N_3 & N_4\\ M_2 & 0 & 0\\ 1 & 0 & 0\end{bmatrix},\quad \mathbf{G}_{23}=\begin{bmatrix}V_5\\ M_3\\ 0\end{bmatrix},$$

$$\mathbf{G}_{31}=[W_1\quad W_2\quad W_3],\quad \mathbf{G}_{32}=[W_4\quad W_5\quad W_6],\quad \mathbf{G}_{33}=[W_7],$$

$$U_1=A_1(\theta_1,\theta_2)(K_1L_1+K_2)+\tfrac{1}{2}K_1M_1,\quad V_1=-2\omega^2(\Delta t/2)^2(K_1L_1+K_2)+A_1(\theta_1,\theta_2)K_1M_1,$$
$$U_2=A_1(\theta_1,\theta_2)K_1L_2+\tfrac{1}{2}K_1M_2+\tfrac{1}{2}K_2,\quad V_2=-2\omega^2(\Delta t/2)^2K_3,$$
$$U_3=\tfrac{1}{2}K_3,\quad V_3=-2\omega^2(\Delta t/2)^2K_4,$$
$$U_4=\tfrac{1}{2}K_4,\quad V_4=-2\omega^2(\Delta t/2)^2K_1L_2+A_1(\theta_1,\theta_2)(K_1M_2+K_2),$$
$$U_5=A_1(\theta_1,\theta_2)K_1L_3+\tfrac{1}{2}K_1M_3,\quad V_5=-2\omega^2(\Delta t/2)^2K_1L_3+A_1(\theta_1,\theta_2)K_1M_3,$$
$$N_3=A_1(\theta_1,\theta_2)K_3,\quad N_4=A_1(\theta_1,\theta_2)K_4,$$
$$W_1=-4\omega^2(\Delta t/2)^2U_1,\quad W_5=-4\omega^2(\Delta t/2)^2U_3,$$
$$W_2=-4\omega^2(\Delta t/2)^2N_3,\quad W_6=-4\omega^2(\Delta t/2)^2U_4,$$
$$W_3=-4\omega^2(\Delta t/2)^2N_4,\quad W_7=-4\omega^2(\Delta t/2)^2U_5,$$
$$W_4=-4\omega^2(\Delta t/2)^2U_2,$$
$$K_1=-\tfrac{A_2(\theta_1,\theta_2)}{A_1^2(\theta_1,\theta_2)+\omega^2(\Delta t/2)^2},\quad K_2=-\tfrac{A_3(\theta_1,\theta_2)}{A_1^2(\theta_1,\theta_2)+\omega^2(\Delta t/2)^2},$$
$$K_3=-\tfrac{A_4(\theta_1,\theta_2)}{A_1^2(\theta_1,\theta_2)+\omega^2(\Delta t/2)^2},\quad K_4=-\tfrac{A_5(\theta_1,\theta_2)}{A_1^2(\theta_1,\theta_2)+\omega^2(\Delta t/2)^2},$$
$$L_3=\tfrac{1}{16+\omega^2\Delta t^2},\quad L_1=16L_3,$$
$$L_2=8L_3,\quad M_1=-4\omega^2\Delta t^2L_3,$$
$$M_2=\tfrac{16-\omega^2\Delta t^2}{16+\omega^2\Delta t^2},\quad M_3=4L_3.$$

The amplification matrix of the SDMM-Newmark composite scheme represented by Eqs. (31)–(34) is given by

$$\mathbf{G}=\frac{1}{\left[\left(3-\frac{3}{2}\theta_1\right)+\omega^2\left(\frac{\Delta t}{2}\right)^2\right]\left[\theta_2+\omega^2\left(\frac{\Delta t}{2}\right)^2\right]}\begin{bmatrix}G_{11} & G_{12}\left(\frac{\Delta t}{2}\right) & G_{13}\left(\frac{\Delta t}{2}\right)^2\\ G_{21}\left(\frac{2}{\Delta t}\right) & G_{22} & G_{23}\left(\frac{\Delta t}{2}\right)\\ G_{31}\left(\frac{2}{\Delta t}\right)^2 & G_{32}\left(\frac{2}{\Delta t}\right) & G_{33}\end{bmatrix},\tag{44}$$

where

$$G_{11}=\left(3-\frac{3}{2}\theta_1\right)\theta_2+\left(\frac{9}{2}\theta_1-7\right)\omega^2\left(\frac{\Delta t}{2}\right)^2,$$
$$G_{12}=3(2-\theta_1)\theta_2+(3\theta_1-4)\omega^2\left(\frac{\Delta t}{2}\right)^2,$$
$$G_{13}=(5-3\theta_1)(\theta_2-2),$$
$$G_{21}=\left(6\theta_1-\frac{3}{2}\theta_2-9\right)\omega^2\left(\frac{\Delta t}{2}\right)^2+\frac{1}{2}\omega^4\left(\frac{\Delta t}{2}\right)^4,$$
$$G_{22}=\left(3-\frac{3}{2}\theta_1\right)\theta_2+\left(\frac{9}{2}\theta_1-2\theta_2-6\right)\omega^2\left(\frac{\Delta t}{2}\right)^2,$$
$$G_{23}=3\left(\frac{3}{2}-\theta_1\right)(\theta_2-2)-(\theta_2-2)\omega^2\left(\frac{\Delta t}{2}\right)^2,$$
$$G_{31}=-\left(3-\frac{3}{2}\theta_1\right)\theta_2\omega^2\left(\frac{\Delta t}{2}\right)^2+\left(7-\frac{9}{2}\theta_1\right)\omega^4\left(\frac{\Delta t}{2}\right)^4,$$
$$G_{32}=3(\theta_1-2)\theta_2\omega^2\left(\frac{\Delta t}{2}\right)^2+(4-3\theta_1)\omega^4\left(\frac{\Delta t}{2}\right)^4,$$
$$G_{33}=(3\theta_1-5)(\theta_2-2)\omega^2\left(\frac{\Delta t}{2}\right)^2.$$

References

[1] F. Armero, I. Romero, On the formulation of high-frequency dissipative time-stepping algorithms for nonlinear dynamics. Part I: low-order methods for two model problems and nonlinear elastodynamics, Comput. Methods Appl. Mech. Engrg. 190 (2001) 2603–2649.
[2] F. Armero, I. Romero, On the formulation of high-frequency dissipative time-stepping algorithms for nonlinear dynamics. Part II: second-order methods, Comput. Methods Appl. Mech. Engrg. 190 (2001) 6783–6824.
[3] K.J. Bathe, Conserving energy and momentum in nonlinear dynamics: a simple implicit time integration scheme, Comput. Struct. 85 (2007) 437–445.
[4] K.J. Bathe, M.M.I. Baig, On a composite implicit time integration procedure for nonlinear dynamics, Comput. Struct. 83 (2005) 2513–2524.
[5] O.A. Bauchau, C.L. Bottasso, L. Trainelli, Robust integration schemes for flexible multi-body systems, Comput. Methods Appl. Mech. Engrg. 192 (2003) 395–420.
[6] O.A. Bauchau, G. Damilano, N.J. Theron, Numerical integration of nonlinear elastic multi-body systems, Int. J. Numer. Methods Engrg. 38 (1995) 2727–2751.
[7] O.A. Bauchau, T. Joo, Computational schemes for nonlinear elastodynamics, Int. J. Numer. Methods Engrg. 45 (1999) 693–719.
[8] P. Betsch, P. Steinmann, Conservation properties of a time FE method – Part II: time-stepping schemes for nonlinear elastodynamics, Int. J. Numer. Methods Engrg. 50 (2001) 1931–1955.
[9] J. Chung, G.M. Hulbert, A time integration algorithm for structural dynamics with improved numerical dissipation: the generalized-α method, J. Appl. Mech. 60 (1993) 371–375.
[10] J.M. Dahl, F. Hover, M.S. Triantafyllou, S. Dong, G.E. Karniadakis, Resonant vibrations of bluff bodies cause multivortex shedding and high-frequency forces, Phys. Rev. Lett. 99 (2007) 144503.
[11] S. Dong, Direct numerical simulation of turbulent Taylor-Couette flow, J. Fluid Mech. 587 (2007) 373–393.
[12] S. Dong, G.E. Karniadakis, DNS of flow past stationary and oscillating cylinder at $Re = 10,000$, J. Fluids Struct. 20 (2005) 14–23.
[13] S. Dong, G.E. Karniadakis, A. Ekmekci, D. Rockwell, A combined DNS-PIV study of the turbulent near wake, J. Fluid Mech. 569 (2006) 185–207.
[14] S. Dong, G.S. Triantafyllou, G.E. Karniadakis, Elimination of vortex streets in bluff body flows, Phys. Rev. Lett. 100 (2008) 204501.
[15] S. Dong, Z. Yosibash, A parallel spectral element method for dynamic three-dimensional nonlinear elasticity problems, Comput. Struct. 87 (2009) 59–72.
[16] C.W. Gear, Numerical Initial Value Problems in Ordinary Differential Equations, Prentice-Hall, 1971.
[17] O. Gonzalez, Exact energy and momentum conserving algorithms for general models in nonlinear elasticity, Comput. Methods Appl. Mech. Engrg. 190 (2000) 1763–1783.
[18] E. Hairer, S.P. Norsett, G. Wanner, Solving Ordinary Differential Equations I, Nonstiff Problems, Springer, 1993.
[19] P. Hauret, P. Le Tallec, Energy-controlling time integration methods for nonlinear elastodynamics and low-velocity impact, Comput. Methods Appl. Mech. Engrg. 195 (2006) 4890–4916.
[20] H.M. Hilber, T.J.R. Hughes, R.L. Taylor, Improved numerical dissipation for time integration algorithms in structural dynamics, Earthquake Engrg. Struct. Dynamics 5 (1977) 283–292.
[21] T.J.R. Hughes, The Finite Element Method, Prentice-Hall, 1987.
[22] T.J.R. Hughes, T.K. Caughey, W.K. Liu, Finite-element methods for nonlinear elastodynamics which conserve energy, J. Appl. Mech. 45 (1978) 366–370.
[23] C. Kane, J.E. Marsden, M. Ortiz, Symplectic-energy-momentum preserving variational integrators, J. Math. Phys. 40 (1999) 3353–3371.
[24] G.E. Karniadakis, S.J. Sherwin, Spectral/hp Element Methods for Computational Fluid Dynamics, second ed., Oxford University Press, 2005.
[25] D. Kuhl, M.A. Crisfield, Energy-conserving and decaying algorithms in nonlinear structural dynamics, Int. J. Numer. Methods Engrg. 45 (1999) 569–599.
[26] D. Kuhl, E. Ramm, Constraint energy-momentum algorithms and its application to nonlinear dynamics of shells, Comput. Methods Appl. Mech. Engrg. 136 (1996) 293–315.
[27] D. Kuhl, E. Ramm, Generalized energy-momentum method for nonlinear adaptive shell dynamics, Comput. Methods Appl. Mech. Engrg. 178 (1999) 343–366.
[28] T.A. Laursen, X.N. Meng, A new solution procedure for application of energy-conserving algorithms to general constitutive models in nonlinear elastodynamics, Comput. Methods Appl. Mech. Engrg. 190 (2001) 6309–6322.
[29] R. Mohr, A. Menzel, P. Steinmann, A consistent time FE-method for large strain elasto-plasto-dynamics, Comput. Methods Appl. Mech. Engrg. 197 (2008) 6309–6322.
[30] N.N. Newmark, A method of computation for structural dynamics, J. Engrg. Mech. Div. Proc. ASCE 85(EM3) (1959) 67–94.
[31] M. Ortiz, A note on energy conservation and stability of nonlinear time-stepping algorithms, Comput. Struct. 24 (1986) 167–168.
[32] K.C. Park, An improved stiffly stable method for direct integration of nonlinear structural dynamics, J. Appl. Mech. 42 (1975) 464–470.
[33] P.M. Pimenta, E.M.B. Campello, P. Wriggers, An exact conserving algorithm for nonlinear dynamics with rotational DOFs and general hyperelasticity. Part 1: rods, Comput. Mech. 42 (2008) 715–732.
[34] C. Sansour, P. Wriggers, J. Sansour, On the design of energy-momentum integration schemes for arbitrary continuum formulations.applications to classical and chaotic motion of shells, Int. J. Numer. Methods Engrg. 60 (2004) 2419–2440.
[35] S.J. Sherwin, G.E. Karniadakis, A triangular spectral element method: applications to the incompressible Navier–Stokes equations, Comput. Meth. Appl. Mech. Engrg. 123 (1995) 189–229.
[36] J.C. Simo, N. Tarnow, The discrete energy-momentum method, conserving algorithms for nonlinear elastodynamics, Z. Angew Math. Phys. 43 (1992) 757–792.
[37] J.C. Simo, N. Tarnow, A new energy and momentum conserving algorithm for the nonlinear dynamics of shells, Int. J. Numer. Methods Engrg. 37 (1994) 2527–2549.
[38] E.L. Wilson, A computer program for the dynamic stress analysis of underground structures, SEL Report 68-1, University of California at Berkeley, 1968.
[39] W.L. Wood, M. Bossak, O.C. Zienkiewica, An alpha modification of Newmark's method, Int. J. Numer. Methods Engrg. 15 (1981) 1562–1566.
[40] W.L. Wood, M.E. Odour, Stability properties of some algorithms for the solution of nonlinear dynamics vibration equations, Appl. Numer. Methods 4 (1988) 205–212.